Doctoral Thesis

Thesis Title

In-situ Observation of Atomic-Scale Defect Evolutions in Pure Al and Al-Cu Alloys by Spherical Aberration-Corrected Transmission Electron Microscopy

Department of Quantum Science and Energy Engineering
Graduate school of Engineering,
TOHOKU UNIVERSITY

CHEN JIAO

Advising Professor at Tohoku Univ.	Professor Yasuyoshi NAGAI
Research Advisor at Tohoku Univ.	
Dissertation Committee Members Name marked with "○" is the Chair of the Committee	○ Prof. Yasuyoshi, NAGAI 1 Prof. Akira, HASEGAWA　2 Prof. Ryuta, KASADA 3 Associate Prof. Koji, INOUE　4 Associate Prof. Kenta, YOSHIDA

TOHOKU UNIVERSITY

Graduate School of Engineering

In-situ Observation of Atomic-Scale Defect Evolutions in Pure Al and Al-Cu Alloys by Spherical Aberration-Corrected Transmission Electron Microscopy

(原子分解能その場電子線照射観察による純 Al と Al-Cu 合金中の格子欠陥挙動に関する研究)

A dissertation submitted for the degree of Doctor of Philosophy (Engineering)

Department of Quantum Science and Energy Engineering

by

CHEN Jiao

January 7, 2022

In-situ Observation of Atomic-Scale Defect Evolutions in Pure Al and Al-Cu Alloys by Spherical Aberration-Corrected Transmission Electron Microscope

CHEN Jiao

Abstract

The atomic-scale point defects, interstitial atoms and vacancies, are produced during irradiation process in materials. It is not so easy to check their existence due to their migration behaviour and atomic-scale size by transmission electron microscope (TEM) until they effect the diffusion of alloy elements or form planar agglomerates which result in properties changing of materials. Therefore, the behaviour of irradiation induced point defects, including interstitial atoms and vacancies, has been investigated from observing the evolution of corresponding planar agglomerates of point defects by using high voltage electron microscope (HVEM) because of its high beam energy, it is easy to induce irradiation defects and obtain higher resolution for defects. However, for the evolutions at atomic scale, such as clustering, growth or disappearing details have not been clearly investigated. Here, *in-situ* observation in spherical aberration-corrected transmission electron microscopy (AC-TEM) is a useful technique for visualizing evolution of individual point defect agglomerates in atomic scale. By using this technique with a 200 kV electron irradiation, the dislocation loop evolutions in pure Al thin films, and the evolution of dislocation loop with precipitates in Al-Cu alloys under electron irradiation are investigated at room temperature (RT).

For the dislocation loop evolutions in electron irradiated pure Al thin film, firstly, an intrinsic faulted loop (stacking fault) formation process is observed at RT under a beam flux of $8.61 \times 10^{20}\ e^{-} \cdot cm^{-2} \cdot s^{-1}$, this faulted loop formed by electron irradiation at the area which shows a low image intensity during prolonged observation time. The low image intensity observed in HRTEM images is speculated to be caused by electron irradiation induced vacancy clusters based on the formation mechanism of vacancy type faulted loops in Al and a referenced Monte Carlo (MC) simulation result. Subsequently, the formed faulted loops grew up toward both ends of itself, after growing to a limited length, finally disappeared in less than 1 frame during prolonged irradiation time at RT. This growth process is explained as the movements of edge dislocations, which located at both sides of the faulted loops, and the driving force of its movements is attributed to electron irradiation induced vacancies and interstitial atoms migrations. In addition, the disappearance mechanism of induced faulted loops is suggested to be due to the vacancy diffusion for strain relaxation by applying a geometric phase analysis (GPA) method. Therefore, for the clustering, growth and disappearance process of electron irradiation induced vacancy type dislocation loops, there shows a direct experimental report in Al at atomic-scale by using the 200 kV AC-TEM technique.

Furthermore, the interaction of dislocation loop with precipitates during evolutions are also investigated in present study. An Al-1.7Cu (at. %) alloys are performed under electron irradiation by 200

kV AC-TEM with a beam flux of $3.74 \times 10^{20}\, e^- \cdot cm^{-2} \cdot s^{-1}$ at RT. Firstly, the Al-Cu 1.7(at. %) alloys with a dissolution state showing a homogeneous image contrast in both thin and thick samples are observed by high angle annular dark field scanning-TEM (HAADF-STEM), and the Cu concentration of the commercial Al-Cu alloy after dissolution treatment is calculated from the energy dispersive X-ray (EDX) spectrum with background noise subtraction to be 1.57 ± 0.02 at. %. Then, during *in-situ* observation, a formation of a/3[111] intrinsic Frank loops is also observed under electron irradiation in dissolved Al-Cu alloys, and this is induced by an asymmetrical climb of the edge dislocation at one side of Frank loops during a prolonged irradiation time. Meanwhile, a considerable strain contrast showing coherent interference between two observed stable edge dislocations is noticed. By combining the experimental results and a referenced theoretical calculation for the asymmetrical climb of the edge dislocation with Burgers vector of a/3[111], the Cu-Cu bonding in Cu coherent precipitates is described as a possible pinning site of the dislocation climb.

Contents

Chapter 1. Background and Objectives

1.1 Atomic-scale defects under electron irradiation

The atomic-scale defects, interstitial atoms and vacancies, known as Frenkel pairs, are produced during irradiation process in materials. Such atomic-scale defects are essential, since the line, plane, and volume defects (such as dislocation loops, stacking faults and voids) evolved from them that are ubiquitous in the crystal materials [1-4]. For example, interstitial atoms would accumulate as dislocation loops at very early stage of irradiation, and such dislocation loops could play an important role in the remaining hardening after thermal annealing in materials [5]; vacancies effecting the diffusion of alloy elements, or form into voids which result in irradiation swelling of materials, was also checked by Wan [6] and Nakai [1, 7], their studies determined that the voids have contribution to the irradiation hardening in nuclear material. Hence, understanding of the line, plane, and volume defects formation process and identification of these atomic-scale defects behaviour become important at the atomic-scale. However, it is difficult to visualize the defect evolutions at atomic-scale by TEM due to the migration behaviour of interstitial atoms and vacancies and their atomic-scale size.

Actually, the behaviour of irradiation induced defects, including interstitial atoms and vacancies, may be investigated from observing corresponding dislocation evolutions [8-10]. A few experimental methods can be used to identify the migration of point defects (interstitial atoms and vacancies) in solid materials. Kiritani et al. [11-12] proposed one method as early as 1970 s, to measure the motion of vacancies in iron by observing dislocation loops evolution, they pointed out that the vacancy migration behaviour is indicated by the size change of dislocation loop which is far down from the surface to

avoid the sample-surface effect. They chose the high voltage electron microscope (HVEM) as observation method, this is because the high-energy electron irradiation generated by HVEM produces pure Frenkel point defect pairs, which is helpful to the understanding of point defects mobility [13-18]. In addition, interstitial atom's migration behaviour under high-energy electron irradiation has also been measured by Yoshida et al. in FCC gold and BCC iron [19-20]. They reported that the nucleation, formation and shrinkage of interstitial type dislocation loops are observed in both gold and iron during high-energy electron irradiation. Meanwhile, Figure 1.1(a) and (b) show the examples of the vacancy type dislocation loops in iron [6] and the interstitial type dislocation loops in Fe-16Ni-15Cr [5], which growing, disappearing and shrinkage during high energy beam electron irradiation are observed using HVEM, respectively. In their studies, they speculated that the behaviour of vacancies and interstitial atoms can be obtained from observing the evolutions of corresponding dislocation loops. However, for the point defect clustering process at atomic scale, they didn't investigate more details. One of the reasons is the sample thickness, the samples about 500 nm thick were used for their studies. As known that at this thickness, the dislocation loops are overlapped along the observation zone axis, instead of single dislocation loop, so the point defect clustering details of these dislocation loops cannot be observed, perfectly. Therefore, one of the necessary conditions for the point defect clustering process is enough thin samples.

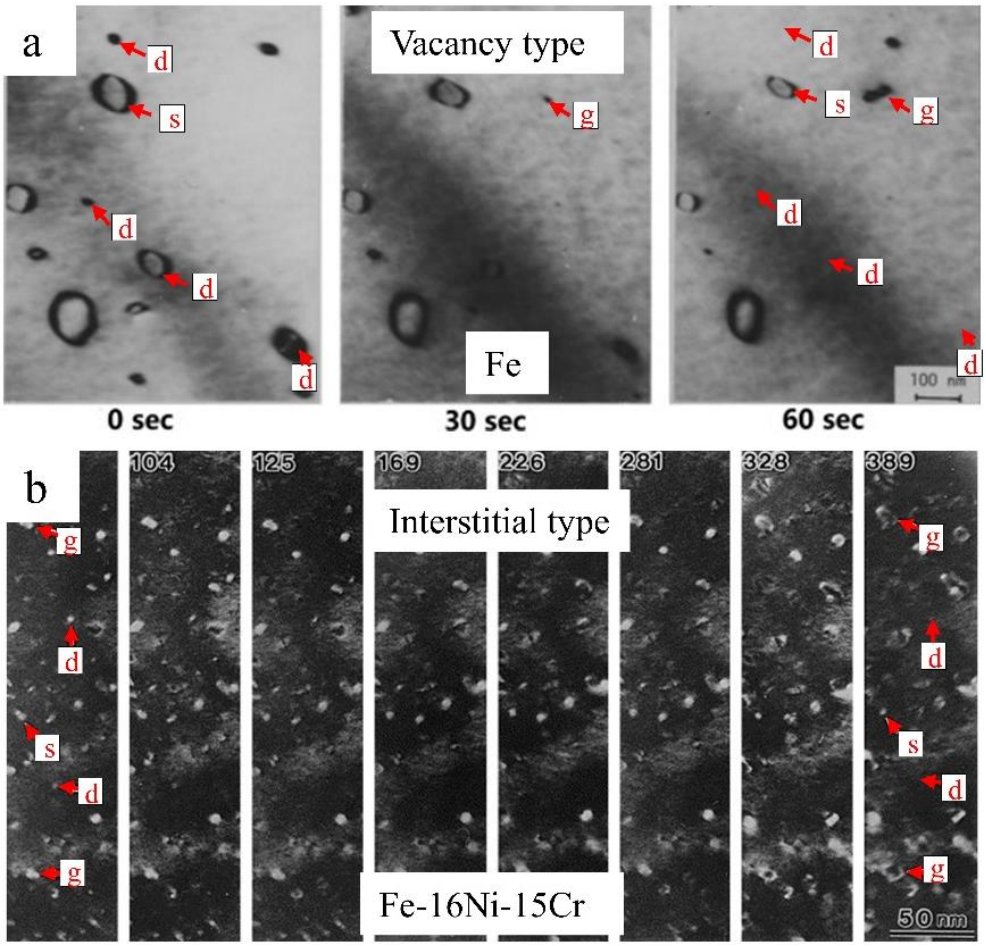

Figure 1.1 (a) Vacancy type dislocation loops in iron, [b] Interstitial type dislocation loops in Fe-16Ni-15Cr [5], which growing, disappearing and shrinkage during high energy beam electron irradiation are observed using HVEM.

1.2 Dislocation loop evolutions in electron irradiated pure Al thin film

For the dislocation loop evolutions, a number of investigations of electron displacement damage in FCC-Al in a high voltage electron microscope also have been reported [21-29]. However, the results are not completely consistent. While Shiraishi et al. [22-23] found that defect clusters in Al (thickness $t = 0.5\,\mu m$) formed and then disappeared under a beam flux of $3.0 \times 10^{18}\, e^{-} \cdot \mathrm{cm}^{-2} \cdot \mathrm{s}^{-1}$ as a result of electron irradiation at 343 K. Wolfenden et al. [25] observed faulted loops in Al (thickness $t = 0.5\,\mu m$) following irradiation at 423 K and Kiritani [26] also observed faulted loops with a beam

flux of $3.8 \times 10^{19}\, e^{-} \cdot \mathrm{cm}^{-2} \cdot \mathrm{s}^{-1}$ at 433 K, respectively. Then, Shiraishi et al. found vacancy loops at temperature lower than 343 K under a vacancy supersaturated environment but the work by Jitsukaga [27] and Kiritani et al. indicated that the loops formed in electron irradiated 99.999 % Al were predominantly of interstitial type, as shown in Figure 1.2 (a) and (b), respectively. While Rao [28] analyzed the perfect loops in Al after irradiation at 293 K and 650 kV and found that 42 % were vacancy type loops and 58% were interstitial one's. In addition to these discrepancies in the observations on defects in electron irradiated Al, it must be noted that Yang et al. [29] also discussed in an Al sample (thickness $t = 0.8{\sim}2\ \mu m$) irradiated at 373 K with a total damage of 0.58 dpa, ~36% of these loops were vacancy and ~64 % of were interstitial type, moreover, the formation of dislocation loops in same sample irradiated at 398 K, the majority of the dislocation loops 90 %, observed in all specimens were faulted and were interstitial type in nature. On the other hand, Shoib and Segall [30] observed that small vacancy clusters produced by quenching in Al shrank and disappeared during electron irradiation. These reviews above show that the nature of electron irradiation damage in Al might has major discrepancies.

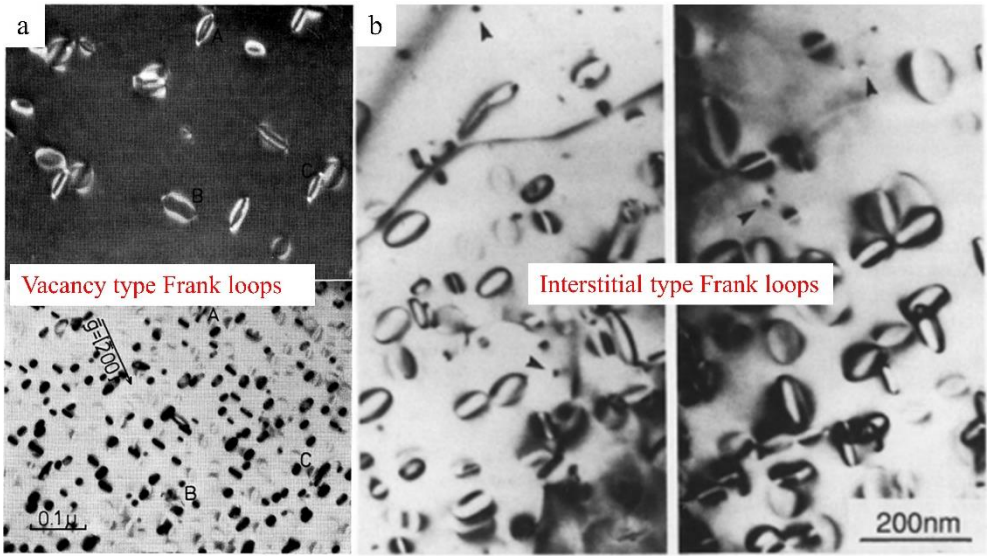

Figure 1.2 Induced Frank loop type in Al under electron irradiation. (a) Vacancy loops under a vacancy supersaturated environment; [b] Interstitial type.

In addition, the above researchers also speculated the behaviour of Al vacancies and interstitial atoms from observing a rapid growth, disappearance and shrinkage of corresponding dislocation loops (vacancy or interstitial type). It is well known that at both ends of dislocation loops, there are two edge dislocations, the growth or shrinkage of dislocation loops can be attributed to the edge dislocation migration, as shown in the Figure 1.3. Meanwhile, from the perspective of edge dislocation migration mechanism, the driving force of edge dislocation migrations can be considered as the electron irradiation induced vacancy and interstitial atom migrations. However, for this explanation, due to the limited observation resolution and the jumping behaviour of Al atoms, resulting in the dynamic formation process (vacancy/interstitial type loops) cannot be clearly identified.

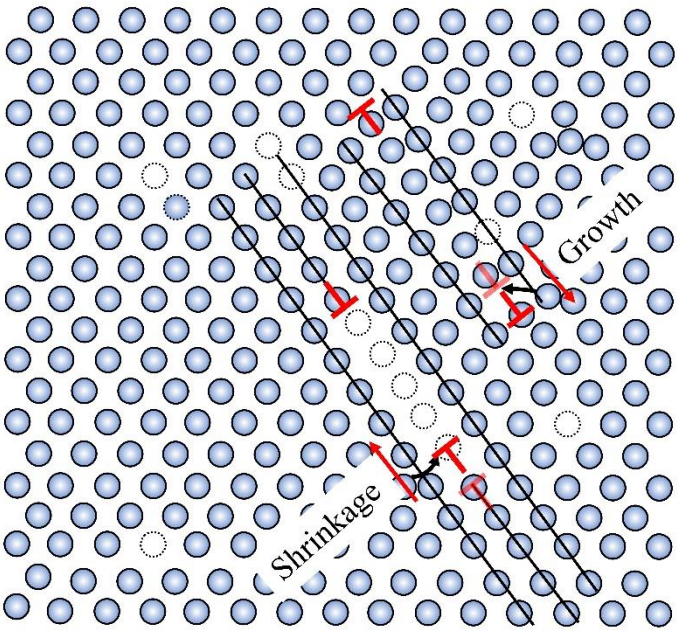

Figure 1.3. Schematic of two edge dislocations located at ends of two dislocation loops

(interstitial and vacancy type).

For the high-resolution observation, it not only depends on electron wavelength but also spherical aberration coefficient C_s in TEM resolution theory. So, an Aberration Corrected-TEM (AC-TEM) also can achieve atomic-scale resolution by C_s correction. Generally speaking, for the AC-TEM, their electron beam energy is not so high as HVEM, such as, the 200 kV AC-TEM, but 200 kV electron irradiation can also knock-on atoms and form interstitial atoms and vacancies in Al.

Therefore, in order to provide a more complete picture of the dislocation loop evolutions due to the edge dislocation migration caused by the migration of vacancy and interstitial atoms during electron irradiation, as an example here, Al was used to quantitatively reveal the evolution of dislocation loop during electron irradiation using 200-kV AC-TEM technique. This is because the displacement threshold energy of Al is 16 eV and the maximum transferable energy is 183 keV for atom displacement under electron irradiation [31-33], 200-kV acceleration voltage is sufficiently high to induce displacement damage in FCC Al. It is also reported by Wolfenden [34-36] that the electron displacement damage was produced in high-purity Al at voltage as low as 200 kV.

1.3 Coherent precipitate hardening

When the edge dislocation movements come into contact with the mechanical properties of materials, one of the main properties of the physical metallurgy is hardness of material. Dislocations as the main carriers of plastic deformation in metallic materials, their slip and climb behaviour affects the source of the structural material hardening. Since the critical shear stress to promote dislocation migration in the most suitable

crystallographic planes in most metals is very low, one strategy to achieve this objective is to insert different types of obstacles in the dislocation glide or climb plane to hinder dislocation migrations [37]. The presence of alloying elements in a solid solution and of precipitates can act as one of obstacles in crystalline samples lead to hardening, termed as solution hardening and precipitation (coherent and incoherent) hardening, respectively, a schematic for this explanation is shown in Figure 1.4. The top side (Figure 1.4[a]) includes two Frank loops and their corresponding edge dislocations, a precipitate in the crystal is displayed in the right side of Figure 1.4(a). In this figure, one of edge dislocations (bottom side) climbs along the climb direction, when the edge dislocation approaches the precipitate, the dislocation is arrested at the precipitates (Figure 1.4[b]).

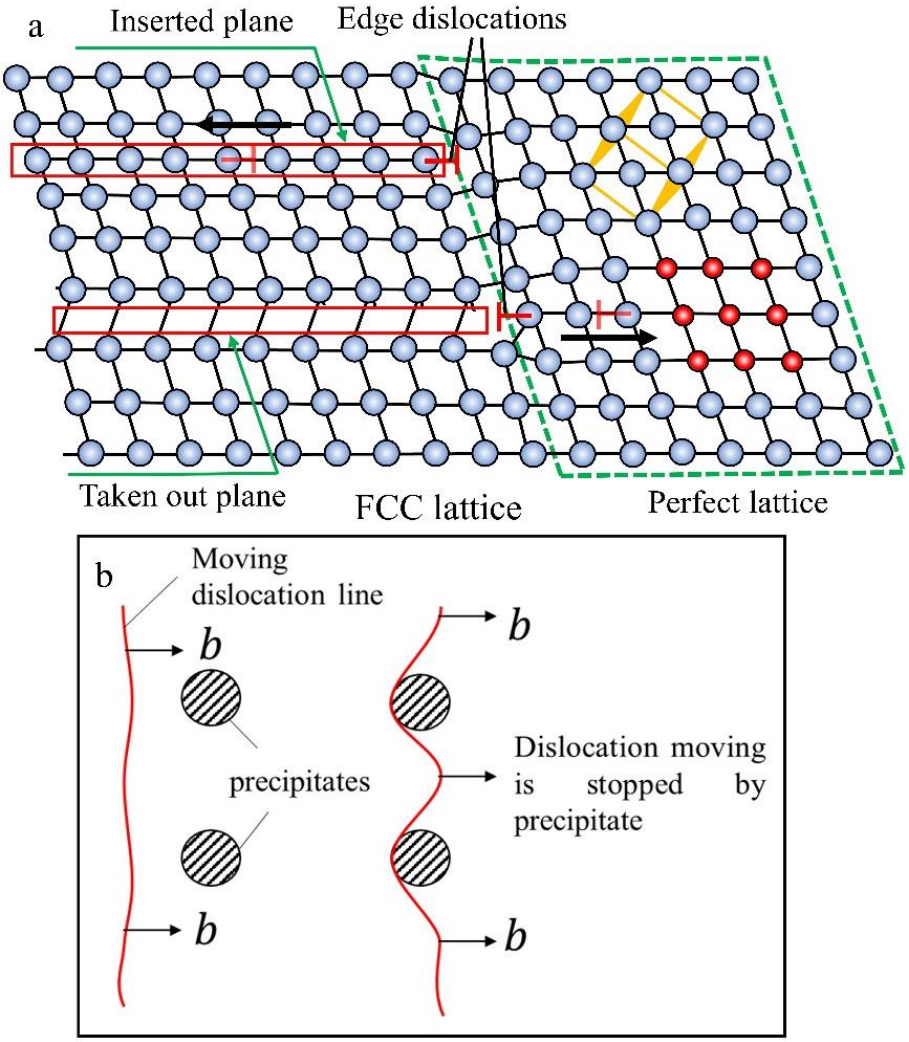

Figure 1.4. Schematic of two edge dislocations and a precipitate in crystal lattice (a) and schematic illustration of their interaction (b).

Based on the hardening mechanism, precipitation hardening due to large incoherent precipitates has been well studied regarding the role of dislocation interaction, obstacle strength by the formation of an Orowan loop and size dependence on mechanical properties [38-42]. Meanwhile, it is reported that in the initial precipitate hardening process, the precipitate hardening effect caused by coherent precipitates can be greater than that caused by incoherent precipitates, which is due to the large number density of precipitates in the early stage, resulting in a large area of lattice strain that can inhibit

the edge dislocation movement [43-45], as shown in the graph of Figure 1.5. However, the coherent precipitate hardening effect caused by local lattice strain could not be accurately evaluated due to the limited lattice stain contrast observation by ordinary TEM technique.

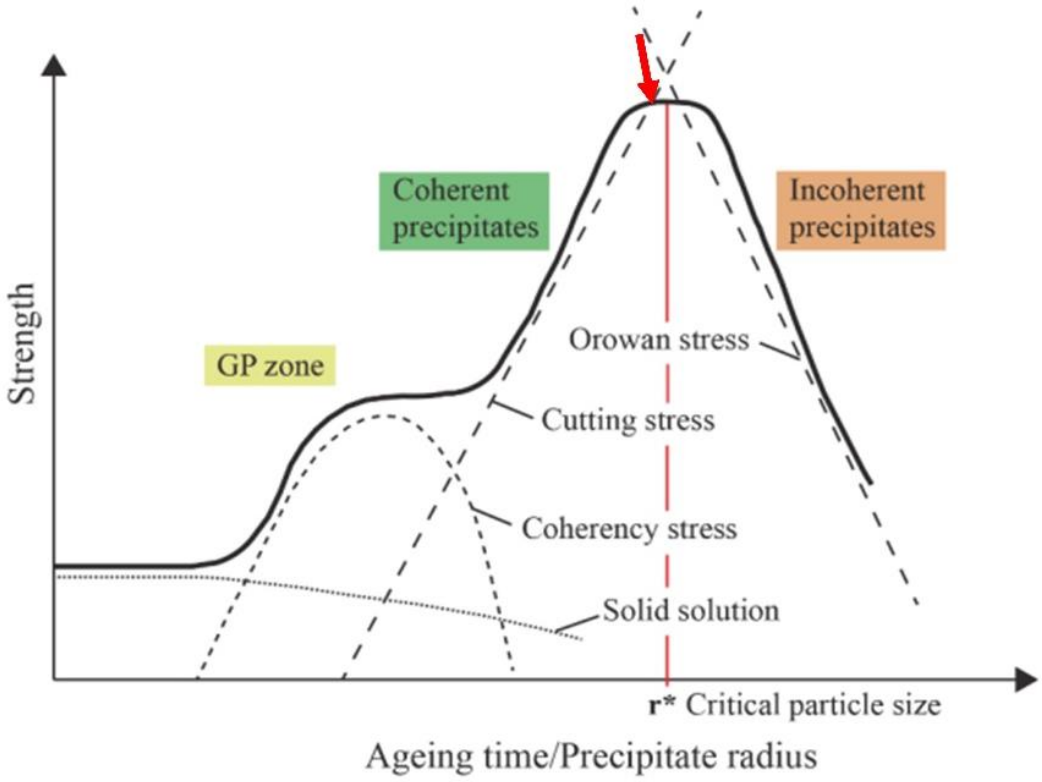

Figure 1.5 Schematic illustration of the precipitate strengthening contributions [44].

Hence, in order to investigate the Frank loop evolutions with precipitates in coherent precipitate hardening mechanism, the secondary phase is necessary for this investigation. Then, the Cu atoms were selected as secondary phase to dope in pure Al becomes Al-Cu alloys. This is due to the very low solubility of Cu atoms in Al, which are easily diffused into Cu clusters (coherent/incoherent) in TEM observations under electron irradiation at RT. Meanwhile, in the study of the precipitate hardening mechanism, lots of experiments and simulations used the Al-Cu alloys as example to investigate the mechanism and obtained several considerable results.

1.4 *In-situ* HRTEM observation

In present study, growing attentions are focused on exploring the evolution of dislocation loops and understanding the dislocation loop evolution with precipitates in coherent precipitate hardening mechanism during electron irradiation. Recently, the rapid development of *in-situ* TEM observation technique makes it possible to directly observe the dynamic evolution process of dislocation loops during electron irradiation [14, 46-48]. Some researchers also have used this *in-situ* TEM observation technique to visualize the microstructural evolution in the FCC lattice of Al, under electron irradiation, elevated temperature [49] and doping second phase precipitates [50] in real space and in nanometer scale. For example, Hale et al. [49] and Martin [51] investigated the dislocation motion in creep process using the *in-situ* HVEM observation technique; Shimotomori and Hasiguti [50] *in-situ* observed the prismatic punching of dislocation loops at second phase precipitates in an Al-1.3Li alloy. *In-situ* electron irradiation of Al at different conditions has been extensively studied using the TEM observation. However, for the evolutions of electron irradiation induced dislocation loops, which is due to the electron irradiation induced vacancy and interstitial atom migrations at atomic scale still not be dynamic observed. Therefore, here for the dislocation loop evolution observation, the *in-situ* AC-TEM observation under an energetic electron beam irradiation has been used to irradiated Al due to the dynamic behaviour of dislocation loops at atomic-scale also can be recorded by this *in-situ* observation technique.

Meanwhile, HRTEM imaging provides an effective technique to characterize material morphology with lattice strain, which is based on the phase contrast. Therefore, here, the HRTEM imaging technique with a new equipment for *in-situ* atomic-scale

observation system was performed to visualize the morphology, size and evolution of the dislocation loops with precipitates in the coherent precipitate hardening mechanism for the Al-Cu alloys.

1.5 Objectives of current thesis

In the present work, *in-situ* HRTEM observation and electron irradiation experiments under TEM were simultaneously carried out for pure Al and Al-Cu alloys at room temperature. The evolutions of dislocation loops in high purity Al and dislocation loop evolution with precipitates in Al-Cu alloys were investigated by real-time. The details are shown as follows:

1. To investigate the evolution of dislocation loops, a high-purity Al was irradiated with electrons using 200 kV AC-TEM at RT and 623 K.
2. To examine and discuss the formation process and disappearance mechanisms of dislocation loops in high-purity Al during electron irradiation.
3. To clarify the dislocation loop evolutions with lattice strain in coherent precipitate hardening mechanism, an Al-1.7 % Cu alloy was irradiated with electrons using 200 kV AC-TEM at RT.
4. To examine and discuss the edge dislocation movements with doping Cu atoms in Al, such as pinning effect in hardening mechanism.

The whole thesis contains 5 chapters:

Chapter 1: **Background and Objectives.** In this chapter, for explaining the importance of dislocation loop evolutions due to the edge dislocation migration in materials and the interaction between dislocation loop and coherent precipitate with lattice strain in

hardening mechanism, relevant fundamental knowledges are briefly introduced. For instance, the driving force of edge dislocation migration can be considered as the electron irradiated vacancy and interstitial atom migrations; interstitial atoms and vacancy in Al can be introduced by 200 kV electron irradiation; a large area of lattice strain inhibits the edge dislocation movement in coherent precipitate hardening mechanism, and the useful *in-situ* observation technique. Such background can lead to the main research topics and the methods to study these points.

Chapter 2: **Experiments and methods**. In this chapter, the main experimental technique used in present thesis are introduced, which includes sample preparation, principle of TEM, phase contrast in HRTEM techniques, *in-situ* observation system and Geometric Phase Analysis (GPA) methods.

Chapter 3: ***In-situ*** **atomic-scale observation of dislocation loops in Al thin films via AC-TEM.** This chapter introduced the first research topic of present thesis (*in-situ* observation of pure Al thin film). Firstly, the dislocation loops produced from atomic scale defects under electron irradiation in a high-purity Al thin film were observed using 200 kV AC-TEM at RT. Before dislocation loop formation, an observed inhomogeneous contrast in the TEM images was observed, then, the observed inhomogeneous contrast was speculated from the result of experiment and discussed using a kinetic Monte Carlo simulation method by Dr. Zhao from Nagai lab., it is proved that it is caused by the irradiation induced vacancy clusters. Finally, the growth process and disappearance mechanism of the electron irradiation induced dislocation loops was also investigated by a Geometric Phase Analysis (GPA) method.

Chapter 4: **Atomic scale observation of dislocation evolution in an Al-Cu alloy with coherent precipitate by *in-situ* irradiation electron microscopy.** This chapter

introduced the second research topic of present thesis (*in-situ* observation of Al-Cu alloys). Firstly, the asymmetric growth process and stability of dislocation loops during prolonged electron irradiation were observed using 200 kV AC-TEM at RT. Then, the different results between pure Al thin film and Al-Cu alloys were discussed by the same GPA method. Meanwhile, the pinning effect in coherent hardening mechanism was investigated at the end of this section. Finally, the interaction between dislocations and coherent precipitates (coherent hardening mechanism) was also discussed using a Molecular Dynamic simulation by Prof. Suzudo from Japan atomic energy agency (JAEA).

Chapter 5: **Summary**. The last chapter of current thesis, a summary of the contents in current thesis are given at the end of this study.

Chapter 2. Experiments and methods

2.1 Sample preparation

2.1.1 Sample fabrication of Al thin films

Al films with the purity of 99.999 % (The Nilaco Corp.) were cut into Φ3-mm discs and then mechanically polished with a dimple grinder (Model 656, Gatan) and abrasive paper discs (#600, #800, #1200 and #2000, Sankyo Rikagaku) until electron-transparent wafers had been obtained. Thereafter, the 3 mm Al discs were electrochemically polished using a twin-jet polishing machine (TenuPol-5) with the mixture of 25 % nitric acid and 75 % methanol at a temperature below 0 °C and the applied potential of 10-12 V.

2.1.2 Sample fabrication of Al-Cu alloys

An Al-1.7Cu (at. %) alloy (Φ3 mm × 35 mm) with a chemical composition of 98.3 at. % Al and 1.7 at. % Cu was provided by Nilaco (No. 572684). The commercial Al-1.7Cu (at. %) alloy was solution-treated at 833 K for 1 h and quenched immediately in ice water. The temperature history of sample preparation for Al-Cu alloys is given as Figure 2.1. Then, thin-film samples (approximately 20 nm thick) were prepared for HRTEM observation by an Ar ion milling technique at RT.

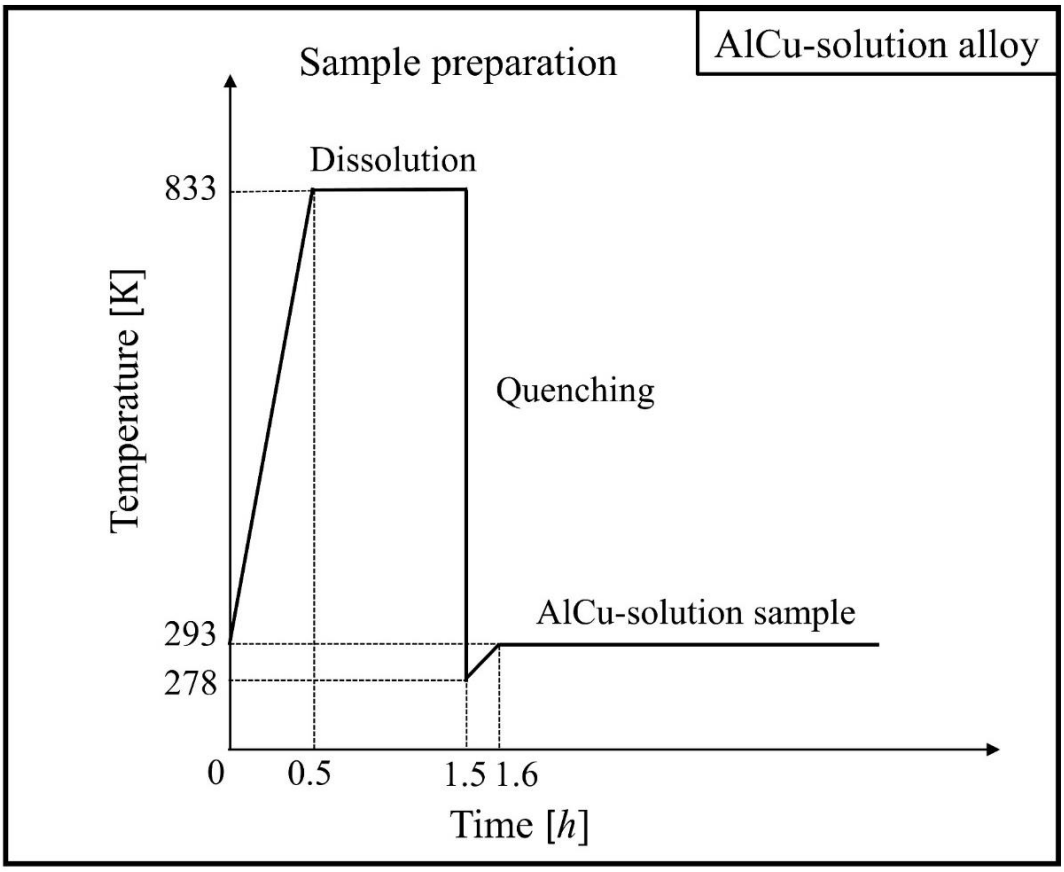

Figure 2.1. The temperature history of sample preparation for AlCu-solution sample.

Moreover, the initial chemical composition of the Al-Cu alloy is shown in Table 1.1. The quenched Al-Cu alloy also was cut into Φ3-mm discs with thicknesses of 1 mm. Subsequently, these discs were mechanically ground to thicknesses ranging from 75 to 95 μm. Then, for the Ar milling technique. The milling voltages were 5 kV for 8 hours; 4, 3, 2, 1 and 0.5 kV for 15 minutes each and 0.3 kV for 30 minutes. The milling angle was maintained at ± 4° for all of voltages. This thin film is referred to as the AlCu-solution sample.

Table 1.1. Composition of the Al-Cu alloy (3 mm 35 mm, Order No. 572684, Cu Φ × concentration; 1.7 at. %).

Chemical composition [at. %]								
Si	Fe	Cu	Mn	Mg	Cr	Zn	Ti	Al
0.590	0.120	1.700	0.300	0.800	0.005	0.017	0.011	Bal.

2.2 Characterization of pure Al thin films and Al-Cu alloys

The *in-situ* HRTEM image observations for Al thin films and Al-Cu alloys were performed on an AC-TEM microscope (ARM 200F, JEOL) with an adjustable spherical aberration coefficient of C_s, in present study, the C_s value was corrected as 0 nm. These samples were observed along the [110] zone axis (close-packed direction) of the FCC Al lattice and Al-Cu alloys. Microstructure evolutions during electron irradiation were recorded as dynamic movements using a high-speed charge-coupled device (CCD) camera (Orius SC200, Gatan) with the average exposure time of 0.05 s. While recording the microstructure evolutions under 200-keV electron irradiation, the current densities measured from a viewing screen (d = 4 cm) are used 423.8 $\rho A/cm^2$ for pure Al thin film and 183.5 $\rho A/cm^2$ for AlCu-solution sample, the beam had a diameter of 70 nm, then the corresponding beam flux of $8.61 \times 10^{20}\ e^- \cdot cm^{-2} \cdot s^{-1}$ for Al thin films and a beam flux of $3.74 \times 10^{20}\ e^- \cdot cm^{-2} \cdot s^{-1}$ for Al-Cu alloys, respectively. Then, the corresponding displacement per atom (dpa) rate of 0.0589 dpa/s and 0.0256 dpa/s for an Al atom displacement energy of 16 eV were obtained at 293 K (RT) [31, 32]. Noted that the different dose rate selections are stochastic in present study. To remove contamination and surface damage, both the Al thin film and the AlCu-solution sample were annealed at 623 K in a high vacuum of 1.2×10^{-5} Pa on a dedicated heating system before *in-situ* electron irradiation at RT.

2.3 Transmission Electron Microscopy

2.3.1 Principle of TEM

Transmission electron microscope (TEM) is a very useful tool in the fields of materials, physics, chemistries and life sciences. Researchers often need to use TEM to obtain the surface (or morphology) and internal information of samples, which is of great help to people to understand the material and conduct further targeted treatment of the materials.

As shown in Figure 2.2, the structure of TEM is quite complex. Only optical systems, such as lenses, aperture, deflectors, and stigmator, are shown in drawing. Various detectors that collect EDS (energy dispersive X-ray (EDX) spectroscopy), EELS (electron energy loss spectrum), BF (bright field), ADF (annular dark field), HAADF (high-angle annular dark-field), SE (secondary electron) signals are not shown in the figure [52]. Due to the different signal generation mechanisms in the interaction between electrons and samples, different detectors have different positions in the TEM, which makes the structure much more complex than shown in the figure.

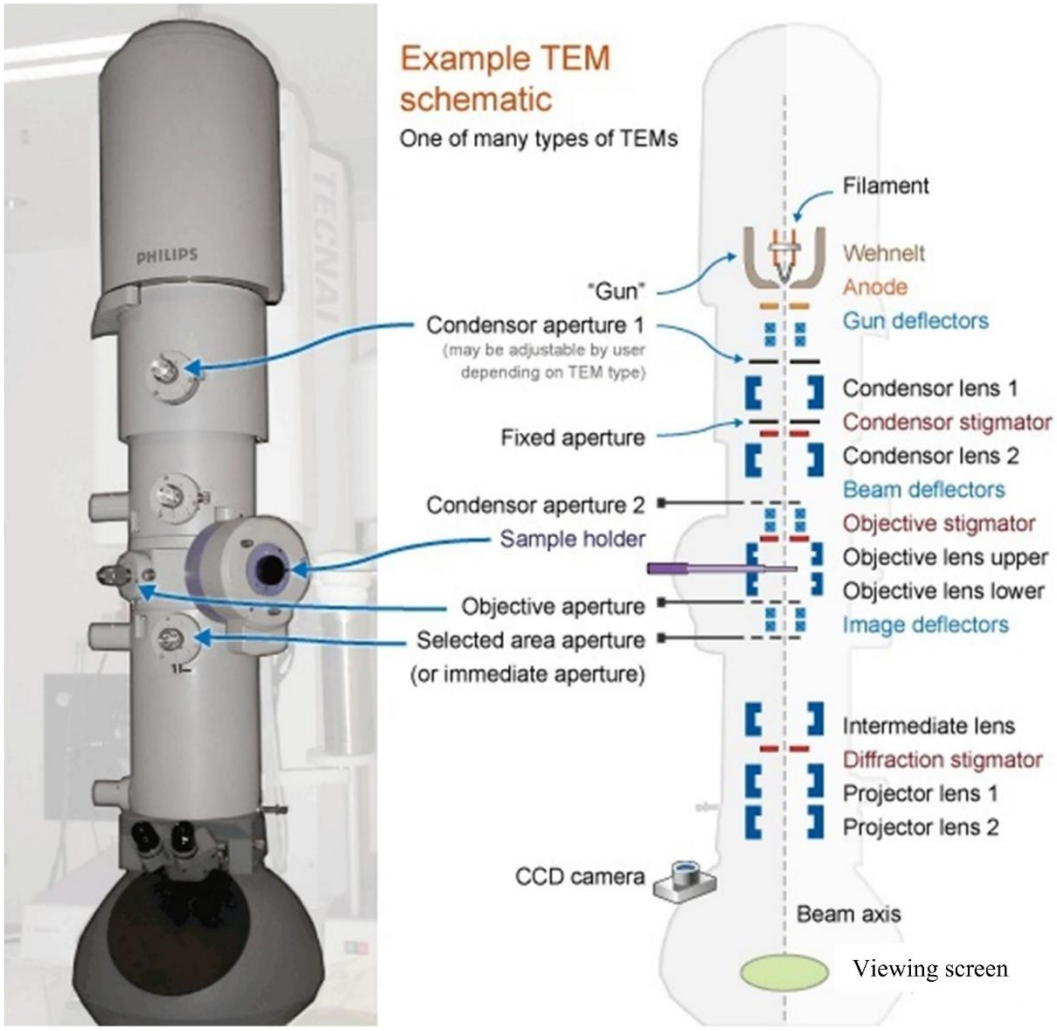

Figure 2.2. Structure of transmission electron microscope [56].

TEM is mainly divided into three parts: illumination system, imaging system and projection system. Take Figure 2.2 as an example to introduce the basic composition of TEM, from top to bottom, the first is the illumination system, which includes the Gun and the Gun deflector. There is an acceleration electric field between the electron gun and the deflector, which is used to accelerate the electrons produced by the electron gun. The acceleration electric field is provided by the acceleration voltage, which can be changed according to the actual situation of the experiment. Electron gun accelerator are used to deflect an electron beam that has just come out of the electron gun, then because the

injected electrons do not always travel perfectly along the beam axis, hence, there often requires preliminary adjustment by the deflector. Then condenser lenses are followed, typically two (#1 and #2), that are used to focus an electron beam that detect interactions with the sample. In this section, a condenser stigmator and a condense aperture also are found. The condenser stigmator is used to perform preliminary calibration of the upper part of the light path between the electron gun and the sample. Generally, the quality of the electron beam directly from the electron gun is not good, coupled with the influence of lens (lens is generally not perfect, there are spherical aberration and chromatic aberration), so it is necessary to use gun deflector and condenser stigmator to adjust the electron beam to make the spot on the sample as uniform as possible. Condenser aperture is a circular disk of light that shields an imperfect part of a light to pass through only a more uniform part in the middle, then a circular spot of light can be obtained in this section.

And when there has the electron beam, then go to the objective part, which is the imaging system. This system is similar to the condenser section, it is with a beam deflector, objective lens, and objective stigmator. The electron beam deflector is used to adjust the position of the beam on the sample. There are two objective lenses, one is objective lens upper, which is used to generate the required electron beam. For example, the lens can be used to control the size of the electron beam spot on the sample surface (the focusing degree can be changed by changing the intensity of the lens when the beam is not parallel). Another is the objective lens lower, which collects the electron beam diffracted by the sample, where the top and bottom are relative to the sample. The objective stigmator were used to eliminate the effects of the objective lenses. There are usually two apertures in the objective lens, one is objective aperture, and the other is selected area aperture. Objective apertures are often used for auxiliary imaging, such as improving contrast in

low-times imaging; The selected area aperture is used primarily in electron diffraction experiments to diffract imaging of a specific region.

Then there is the projection system, starting with the intermediate lens, a lens that controls the imaging mode. By changing the intensity of the lens, it can be switched between normal imaging mode and diffraction mode. Then a stigmator is used to eliminate the effects of the intermediate lens. Then there are two projective lenses, which are used to project the resulting image onto the projector for observing.

2.3.2 Phase contrast imaging in TEM

As the name suggests, the phase contrast imaging is mainly achieved through coherence and is therefore closely related to the phase of the scattered electron beam. This imaging mode is mainly used in TEM mode. In this imaging mode, the incident electron beam is parallel, which means that the high resolution image is obtained from the interference imaging of scattering electron beam in this case. Unlike diffraction contrast images, the high resolution ‘structural’ images are obtained by allowing several diffracted beams to contribute to the image. Usually, the specimen is tilted to a low-index ‘zone-axis’ orientation. Then a large objective aperture is used to select a number of beams to form the image. The image is recorded under a carefully selected defocus condition, and great care is taken in correcting astigmatism. This is made easier on modern instruments by the provision of a high-magnification TV system, or even on-line Fourier analysis. Exposure times are kept to a minimum by the use of sensitive films and accelerated film development, as for weak-beam imaging, or intensified video or CCD cameras. The resulting ‘structural’ image may, under certain conditions, resemble the projected charge

density of the object. Therefore, the HRTEM images used to characterize material morphology. In this case, the light path in the electron microscope is actually an optical transmission function, which transmits the information of the sample to the detector for imaging. Meanwhile, for the high resolution of images, since the lenses are generally not perfect, there are spherical aberration and chromatic aberration, in order to improve the imaging resolution, it is necessary to optimize the optical transmission function of the imaging system [53].

2.3.3 Spherical Aberration corrected-TEM

As described before, due to the existence of aberration (spherical aberration, astigmatism, coma aberration and chromatic aberration), no optical or electromagnetic lens system can be perfect. Spherical aberration is a kind of aberration, which is one of the main factors affecting the TEM resolution. In optical lenses, convex lenses and concave lenses can be combined to reduce the defect that all lights cannot converge to a focus due to the strong converging ability of convex lens edge and weak converging ability of convex lens center. For electromagnetic lens, there are no concave lenses, spherical aberration has become the most important and difficult problem affecting the resolution of TEM. In the 2000s, Rose et al. reported that the sphericity correction device can be used and act as a concave lens to correct the spherical aberration of TEM, which is called the spherical aberration corrected TEM [54-56]. Because TEM is divided into ordinary TEM and STEM for fine structure imaging, the spherical aberration corrected TEM can also be divided into AC-TEM (spherical aberration corrector device installed at the objective lens position) and AC-STEM (spherical aberration corrector device installed at the condenser lens position). In addition, two correctors are also installed on one TEM

simultaneously to correct convergence beam and image with double spherical aberration correction.

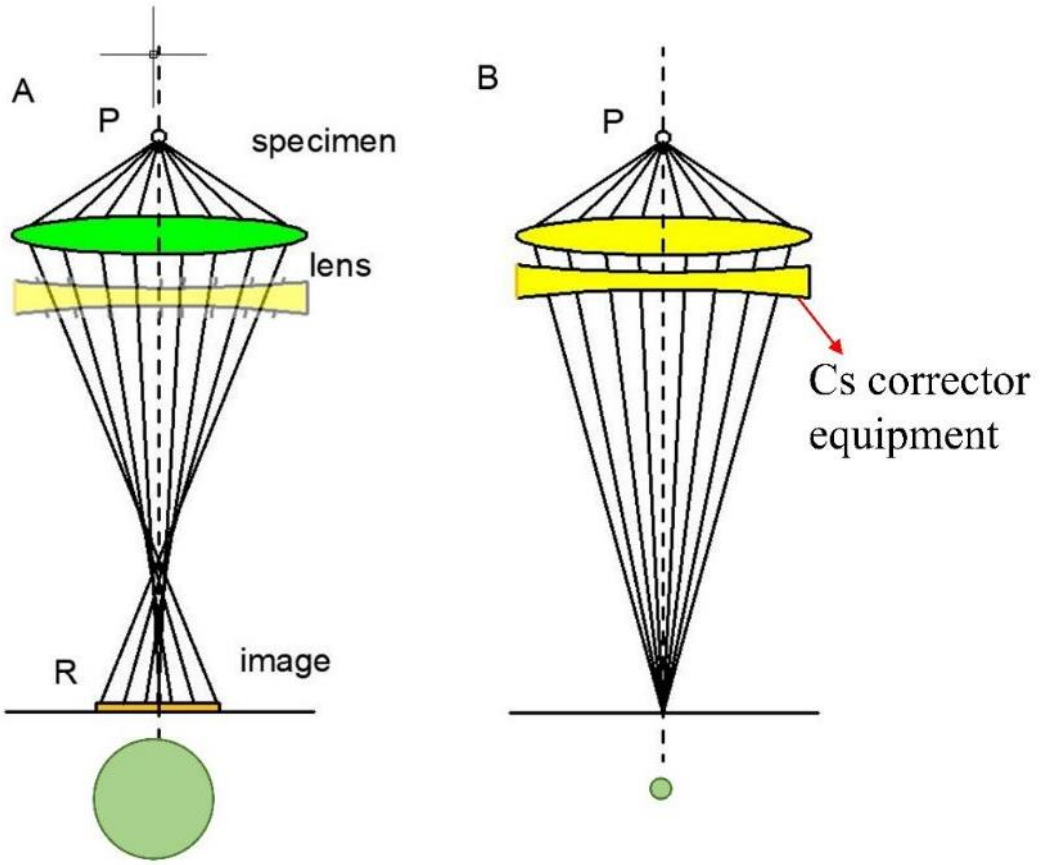

Figure 2.3. Schematic diagram of Cs-TEM without Cs-corrected (left side) ,with Cs-corrected (right side) [60].

As shown in Figure 2.3, compared with traditional TEM, the resolution of AC-TEM is significantly improved due to the effective reduction of aberration. The resolution of traditional TEM and STEM is in nanometer and subnanometer level, while the resolution of AC-TEM and AC-STEM can reach angstrom and subangstrom level [57]. The improved resolution means finer and more accurate structural characterization of materials. Therefore, the AC-TEM here is performed to investigate the evolution of dislocation loops in pure Al thin film and Al-Cu alloys.

2.4 *In-situ* observation technique

An *in-situ* observation system [58] was used in the current study. Figure 2.4 shows the new equipment of *in-situ* atomic-scale observation system performed in this study. This system consists of a heating-pot type sample holder (b) and a thermal controlling box with a proportional integral differential (PID) controller (a). The pure Al thin film and Al-Cu alloys for atomic-scale observation were operated by an AC-TEM with a CETCOR image corrector (CEOS GmbH) and thermal field emission gun, at the acceleration voltage of 200 kV, as shown in Figure 2.4(c). Furthermore, the microstructure evolution with the high spatial resolution of HRTEM was recorded as a movie file using a charge-coupled device (TV-rate CCD camera, Orius SC 200TM, Gatan Inc.) system with 20 frames/s. The system was able to achieve the information limit of 1.5 Å and the point resolution of 2.0 Å for TEM images under isothermal annealing at 623 K.

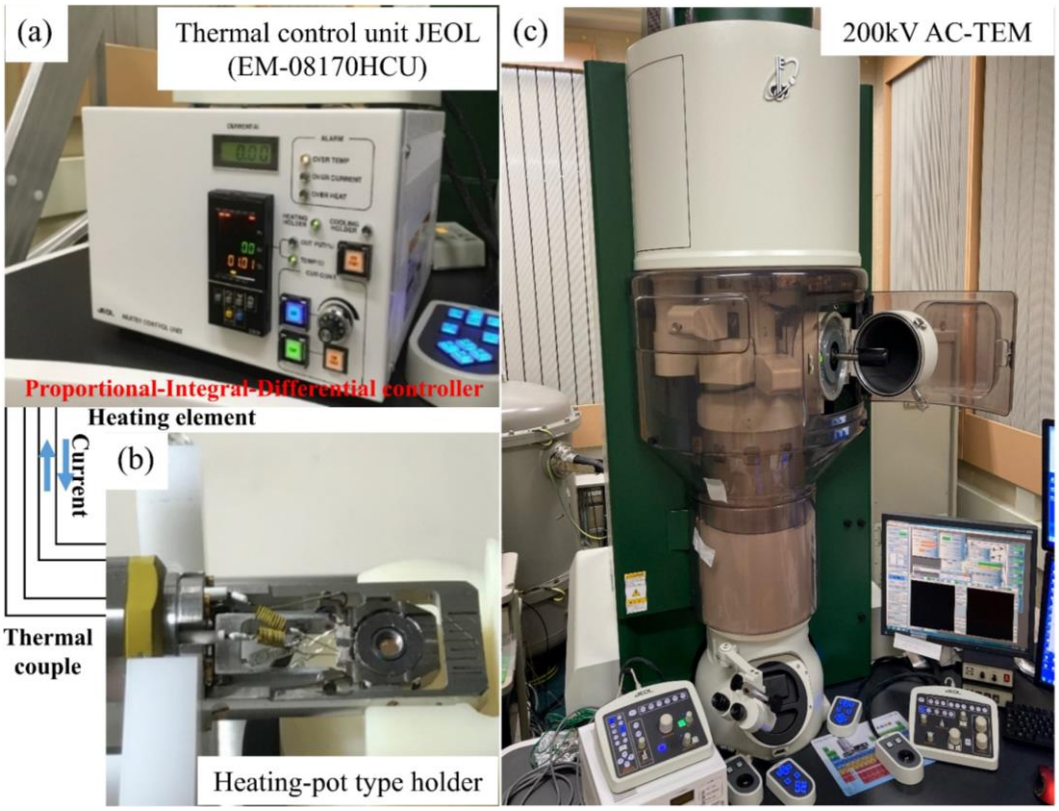

Figure 2.4. An *in-situ* observation system used in the current study. (a) A thermal controlling box with a PID controller; (b) A heating-pot type sample holder; (c) An AC-TEM with a CETCOR image corrector and thermal field emission gun operating at 200 kV.

2.5 Geometric phase analysis (GPA) methods

Defects and associated strain fields are of considerable importance in affecting the lattice structure. There needs an effective method to investigate the deformation in HRTEM images and can be used in various fields. The Geometric phase analysis (GPA) method, developed by Hytch in 1997 [59-61], has become a widely used tool for measuring the deformation in HRTEM images. In recent years, the GPA method combined with advanced manufacturing technology of high-frequency grating has expanded into a full-field, no-contact, non-invasive and simple deformation measurement method. Based on the phase difference of grating images before and after deformation, the phase information is extracted by Fourier transform. In measurements, displacement and strain are closely related to the fundamental frequency of the image, so it is very important to obtain the fundamental frequency accurately. Fast Fourier Transform (FFT) algorithm, generally use in GPA method to save calculation time. Here is a brief introduction of the FFT GPA process, see [62] for details. A flowchart highlighting the main FFT GPA process is shown in Figure 2.5.

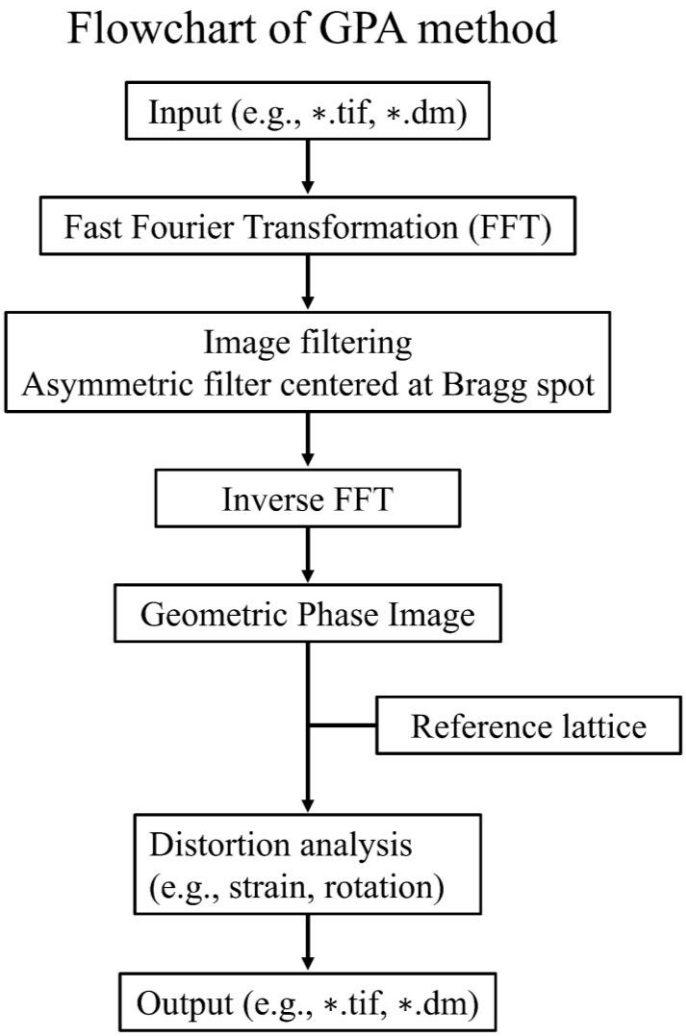

Figure 2.5. The flow chart of the FFT GPA method.

The FFT GPA is based on the relationship between the displacement and the phase difference, which can be directly analysis any displacement field distorting in HRTEM image relative to the reference lattice distortion. In the GPA method, usually in the field of HRTEM, the reference phase selection from HRTEM images of the regular arrange atoms area, and then the deformed phase images can be obtained at the deformed position of the target. This method is applied to the measurement of displacement fields around an edge dislocation in Si and the accuracy is 0.03 Å [63]. In this case, the displacement can be measured by analyzing the lattices between reference area and deformation area, and

this technique also has been utilized to measure the deformation at macro and microscale [64-66]. For example, Li Luying et al. [67] used the GPA method to obtain the strain field distributions at InAs partial dislocation cores associated with Z-shape faulted dipoles, as shown in Figure 2.6. They reported that the dislocation cores are source of strain inversion, by overlapping the HAADF images obtained from experiment, there is an edge dislocation with negative component in Figure 2.6(c) and an edge dislocation with positive component is shown in Figure 2.6(d). It means that the local phase can be directly related to any strain field in the HRTEM images with respect to the reference lattice.

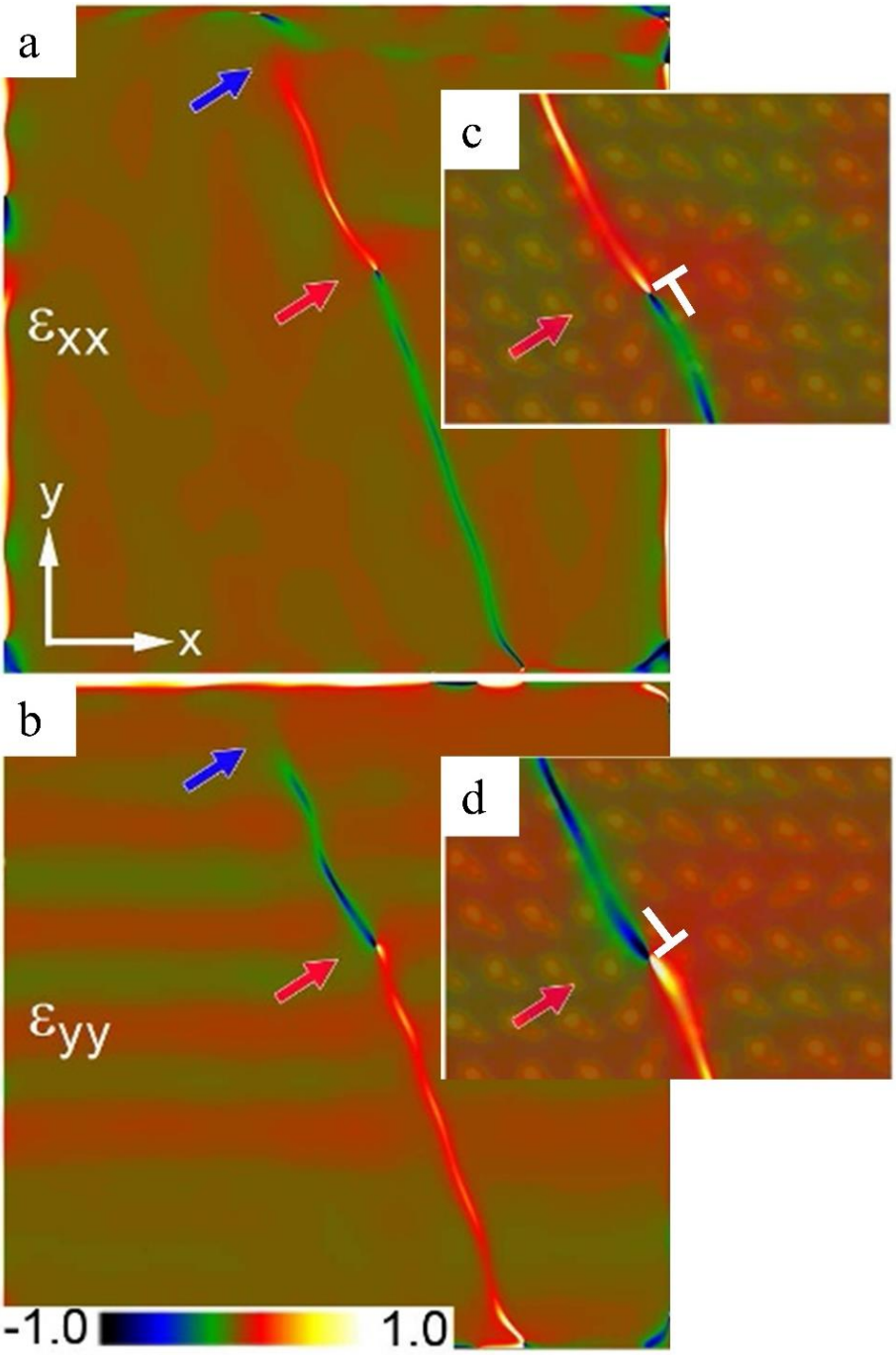

Figure 2.6. Geometric phase analysis based on a HAADF image. The results of the normal strain components $\varepsilon_{xx}$and ε_{yy} are presented in (a) and (d), respectively.

Therefore, a GPA program compatible with Digital Micrograph was used to calculate the lattice strain maps around the dislocation loop, and the results of normal strain components along horizontal and vertical directions of dislocation loops are applied

during *in-situ* HRTEM observation.

Chapter 3. *In-situ* atomic-scale observation of dislocation loops in Al thin films via AC-TEM

3.1 Experimental procedure

3.1.1 Material

In this experiment, this study examined only one kind of material, the pure Al thin films with the purity of 99.999 % (The Nilaco Corp.). The sample fabrication of Al thin films for *in-situ* HRTEM observation have been introduced in section 2.1 as shown in Chapter 2.

3.1.2 *In-situ* HRTEM observation

The microstructure evolution with the high spatial resolution of HRTEM was recorded as a movie file using a charge-coupled device (TV-rate CCD camera, Orius SC 200^{TM}, Gatan Inc.) system with 20 frames/s. Using the phase contrast imaging technique described in Chapter 2.4.2, it is able to visualize the atomic column morphology changing caused by electron irradiation under 200 kV AC-TEM observations. When recording the microstructure evolutions under 200 keV electron irradiation, the beam flux of $8.61 \times 10^{20}\ e^{-} \cdot cm^{-2} \cdot s^{-1}$ was used, which corresponded to the displacement per atom (dpa) of 0.0589 dpa/s that was sufficient to induce Al vacancies for the displacement energy of 16 eV at 293 K. Additionally, the temperature history of all the videos recording for *in-situ* observation is given as Figure 3.1, and the experimental equipment used for *in-situ* observation is shown in Figure 2.4.

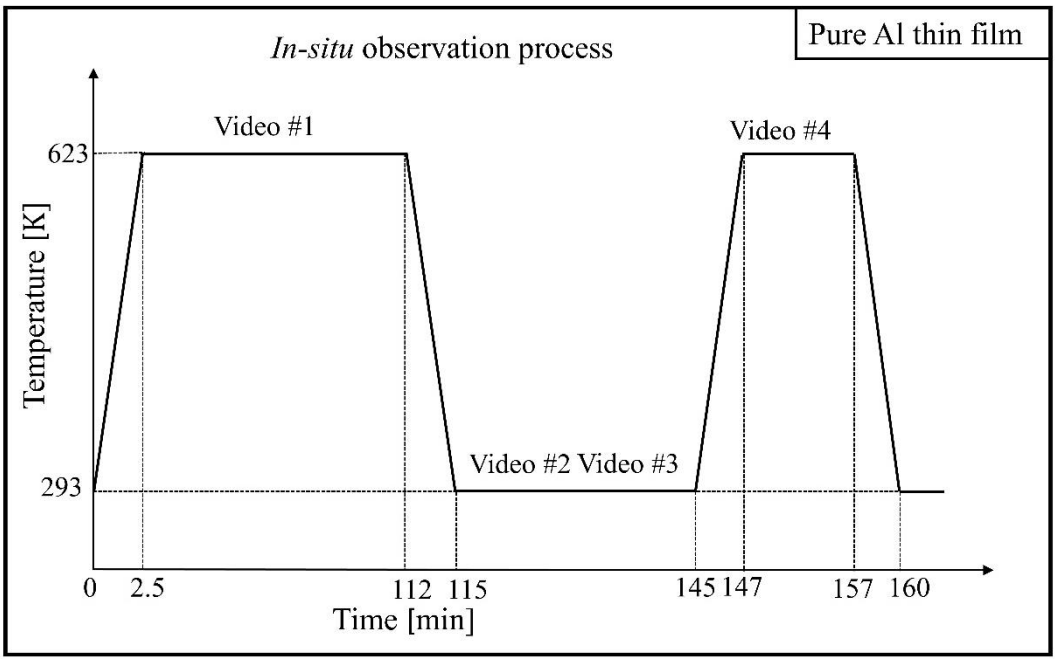

Figure 3.1. Temperature history of all videos recording for *in-situ* observation of pure Al thin film.

3.1.3 Removing contamination using *in-situ* annealing at 623 K

Before *in-situ* observation at RT in the present study, the Al thin film prepared by electrochemical polishing, which has amorphous AlO_x layer and initial lattice defects was *in-situ* annealed within approximately 6,000 s at 623 K temperature under the same beam flux as at RT, firstly.

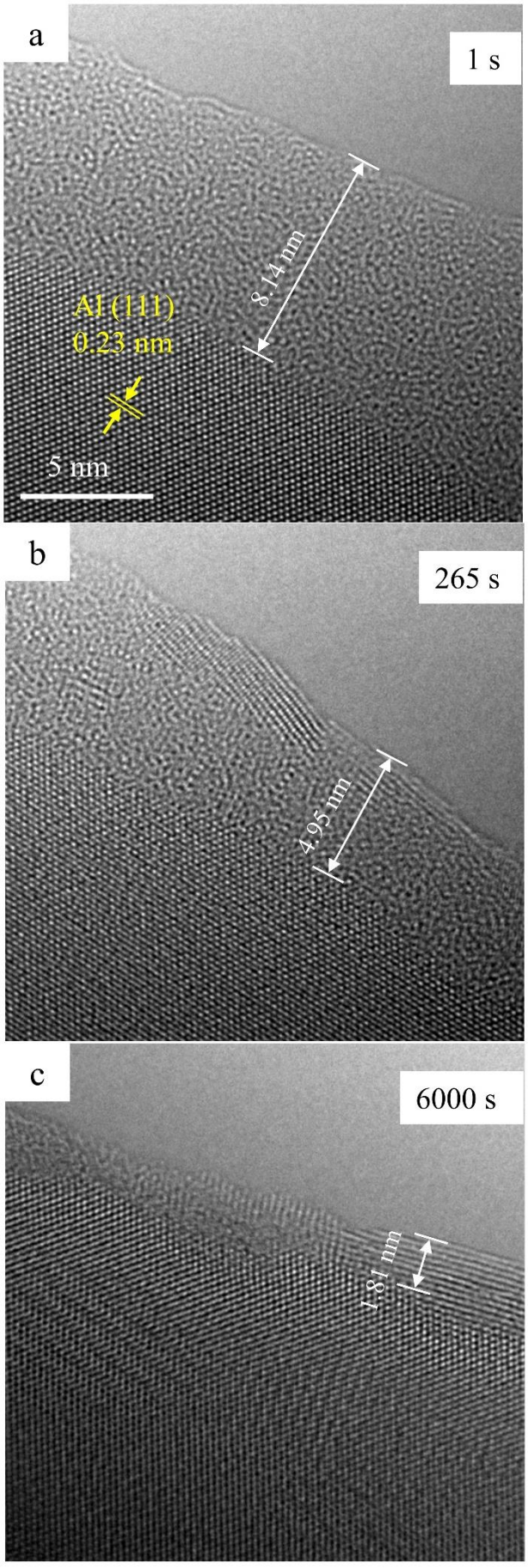
a
1 s
8.14 nm
Al (111)
0.23 nm
5 nm
b
265 s
4.95 nm
c
6000 s
1.81 nm

Figure 3.2. HRTEM images captured from video #1 at different times under electron irradiation at 623 K.

Figure 3.2 shows the HRTEM images of the edge of the Al thin film along [110] axis captured from video #1 for 1, 265, and 6,000 s after temperature raised to 623 K. During the *in-situ* annealing, the amorphous layer (≈8.14 nm) in Figure 3.2(a) decreased to 1.81 nm for 6,000 s, as shown in Figure 3.2(c). As one technical side of the present *in-situ* electron irradiation at RT, the Al thin film was hold under electron irradiation at 623 K for 6,000 seconds and keeping the spatial resolution in the video #1. By the *in-situ* electron irradiation/heating at 623 K, the amorphous re-deposition layer, contamination and surface roughness due to sputtering and some initial lattice defects, which had been produced through electrochemical polishing were completely removed. Meanwhile, this process can be seen as a crystallisation of amorphous Al. As the one of necessary conditions for dislocation loop evolution observation, the requirements of enough thin sample and clean surface are obtained by the *in-situ* electron heating at 623 K.

3.2 Experimental results

3.2.1. Aggregation of point defect clusters in Al thin film at RT

After removing the contamination at 623 K annealing, the *in-situ* observation with electron irradiation at RT was performed. In general, point defect number increases when prolonging electron irradiation time while keeping other parameters (e.g., temperature and beam flux) the same and resulting point defect aggregation. Finally, in thin films, these aggregating point defects could form extended defects, such as line, plane or volume defects. Figure 3.3 shows the images captured at 0, 60, 90, 149, 150 and 250 s during the *in-situ* electron irradiation, which were captured from the video #2 recorded at the

optimum defocus of 5 nm under $C_s = 0\ nm$. From this recorded video, it is clearly to see that an extended defect, which is a stacking fault (SF) on the (111) plane was observed during *in-situ* electron irradiation at RT, as shown in Figure 3.3(e).

This generated SF can be considered to have been caused by the insertion or extraction of a disc of atoms from the matrix. Because every segment has a pure edge character and the Burgers vector is $b = 1/3\,[111]$, then this type of SF cannot slip but instead can climb, and it is called a Frank sessile loop or a faulted loop. It is well known that at both ends of that faulted loop, there are two edge dislocations, the growth or shrinkage of faulted loops can be attributed to the corresponding edge dislocation migrations. In this case, the growth process of the observed faulted loop is shown in Figures 3.3(e)-(f). During the continuous observation, based on a Burgers circle, the generated faulted loop can be defined as intrinsic faulted loop, which is the vacancy type dislocation loops. Since the irradiation induced interstitial atoms diffuse faster than vacancy, there are easy to be absorbed by sink on surface, leading to a low concentration in thin film sample, then the interstitial atoms are neglected in present study. Therefore, this faulted loop generation and growth process are qualitatively similar to the intrinsic SF formation process; therefore, it can be looked to the following theory [68]: in particular, at the beginning of the electron irradiation, the irradiation induced vacancies tend to aggregate and form a faulted loop, then during the continuous irradiation process, irradiation induced more vacancies migrate towards the faulted loop to release the stress caused by the faulted loop. Once the vacancies approach, the edge dislocations at both sides of the faulted loop climb and make the growth of the faulted loop on the (111) plane. Thus, this study can reasonably assume that the driving force of edge dislocation migration can be considered as the electron irradiated vacancy migrations, a schematic about this explanation is shown

in Figures 3.3(g)-(i).

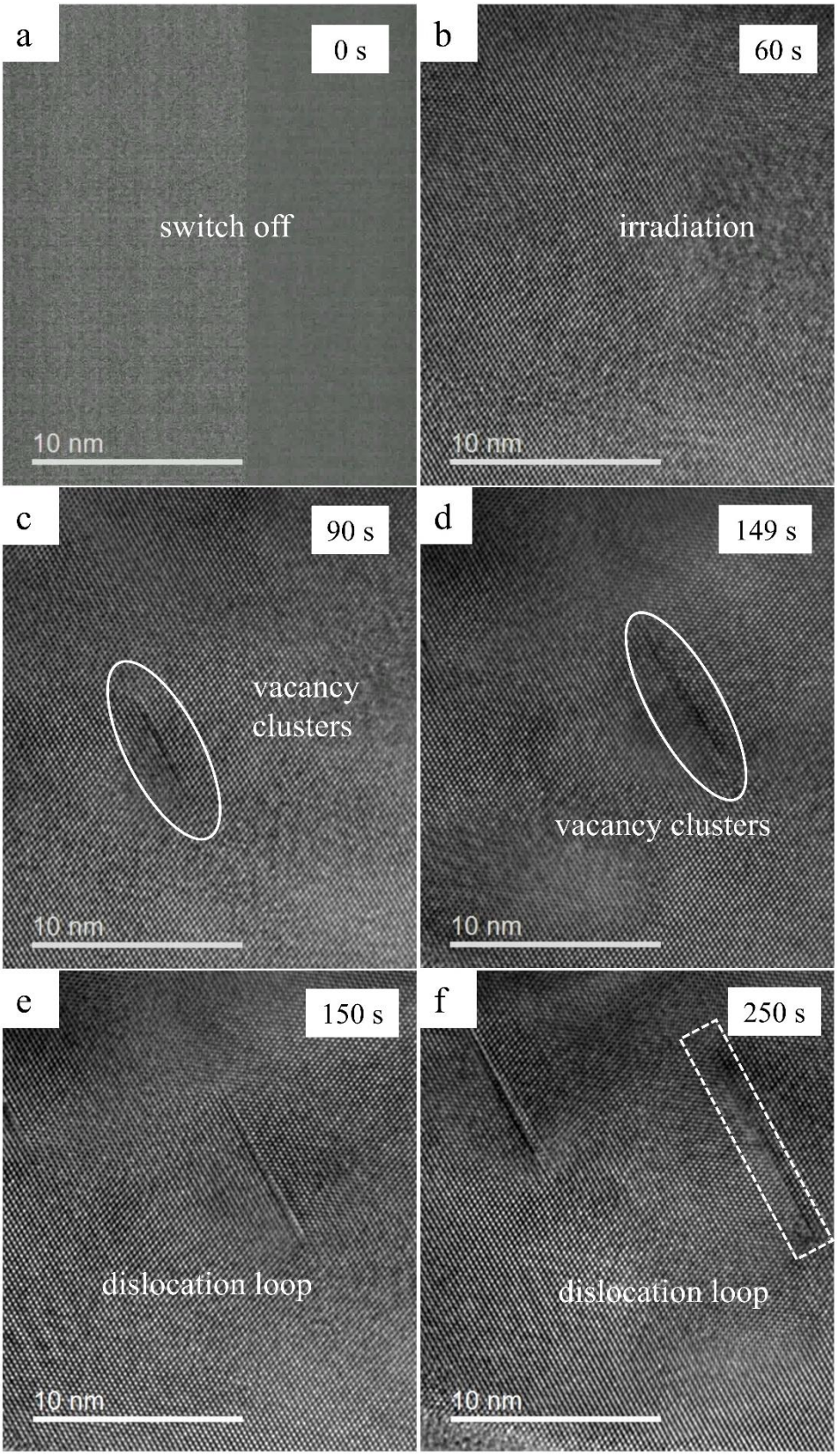

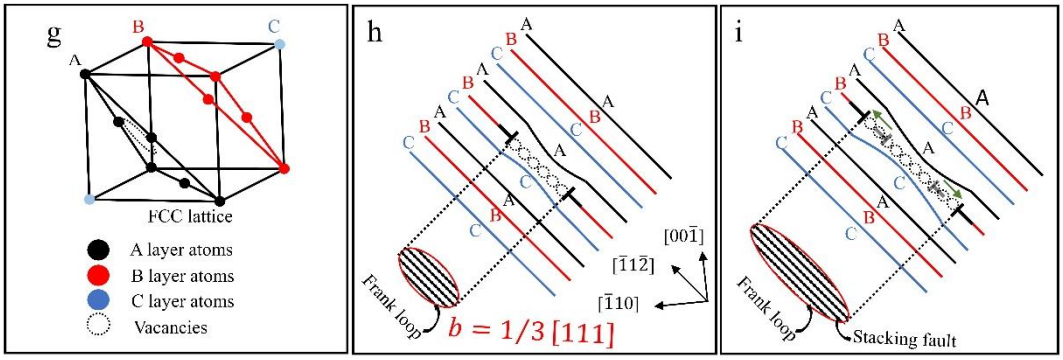

Figure 3.3. (a-f) *In-situ* HRTEM images taken at room temperature, including (a-e) the appearance process of an intrinsic SF on the (111) plane, (e-f) SF growth process, (g-i) schematic of a faulted loop formation and growth mechanism.

3.2.2. Analysis of faulted loop formation process in Al thin film

Furthermore, a SF as a dislocation loop was observed after observing an inhomogeneous image contrast during the *in-situ* observation in section 3.2.1, then something interesting was found from this experimental result, Figures 3.4(a)-(c) show the images captured at 1, 60 and 90 s during the electron irradiation, which were obtained from the same video #2. From the three images, no significant difference was presented between the images taken at 1 and 60 s, as shown in Figures 3.4(a) and (b), whereas the image at 90 s exhibits a darker image intensity for the atomic columns. This is illustrated by the red line in Figure 3.4(c) and resulted in an inhomogeneous contrast among the atomic columns during the electron irradiation. To understand this darker image intensity, Figures 3.4(1)-(3) show the intensity profiles of atomic columns of the three red lines drawing in Figures 3.4(a)-(c), respectively. It can be described that for the image captured at 1 s, the intensity profiles of all the atomic columns were almost identical as almost no vacancies or interstitial defects were produced at the beginning of irradiation, as shown

in Figure 3.4(1). As the observation time increased to 60 s, these intensity profile peaks became unequal, with a number of them decreasing, as indicated by red arrows in Figures 3.4(b) and (2). This was due to additional vacancies being induced during this period. At 90 s, all the peak intensity profiles had been drastically reduced compared with the initial one of Figure 3.4(1). These three intensity profiles indicate that as the irradiation time increased, the intensity peaks of the atomic columns decreased continuously until reaching extremely low values.

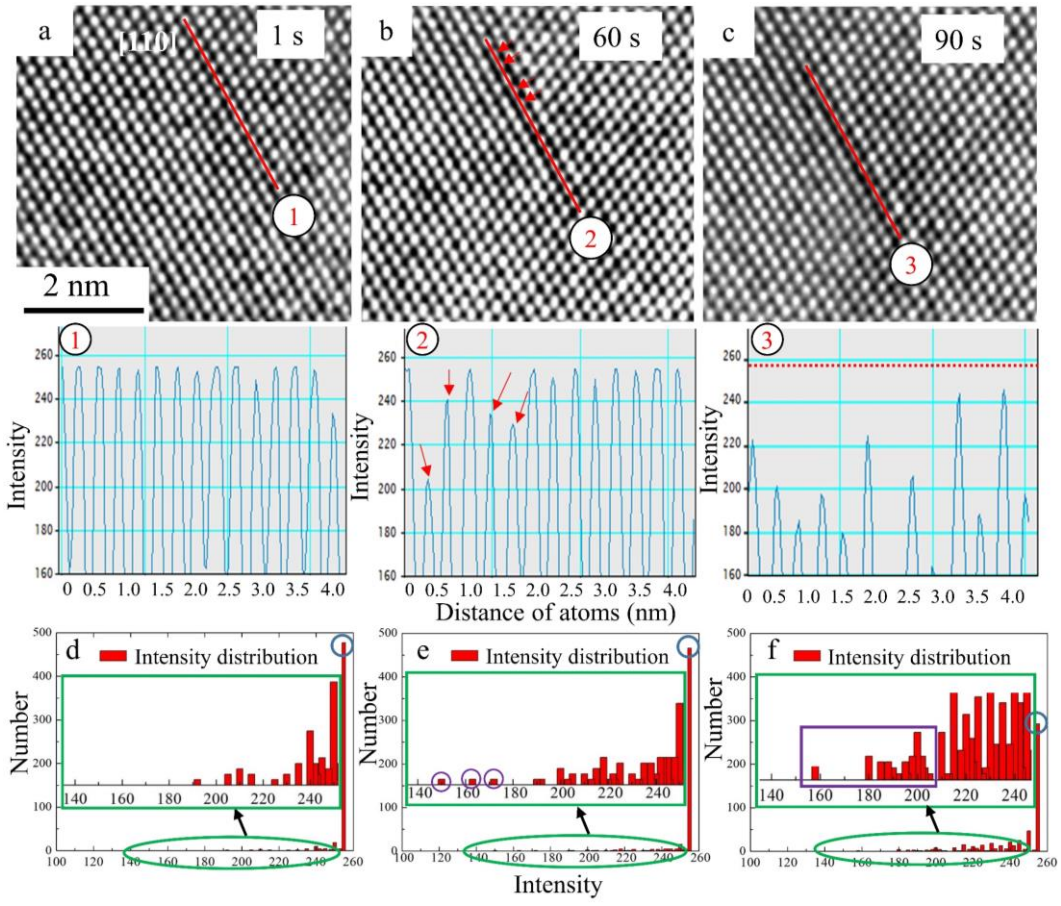

Figure 3.4. (a-c) High-resolution transmission electron micrographs taken at 1, 60 and 90 s during the electron irradiation at RT. (1-3) Intensity peak profiles of the atom columns of the red lines from (a-c). (d-f) Distribution of the intensity peak values of all the atomic columns from (a-c).

To further investigate this strong dependence of the atomic column intensity peak values on the electron irradiation time, Figures 3.4(d)-(f) present the distributions of the intensity peak values for all the atomic columns in the images shown in Figures 3.4(a)-(c). At the beginning of the observation (1 s), the data were concentrated in the high-value region, *i.e.*, almost all the intensity peak values were relatively high, which is consistent with the corresponding intensity peak profile (Figure 3.4[1]). As the observation time increased to 60 s, a number of new bars appeared in the low-value region (purple rings in magnified images of Figure 3.4[e]), which were not present in Figure 3.4(d). At 90 s, almost all the bars in the low-value region (purple rectangle in Figure 3.4[f]) increased, and many of those in the higher-value region decreased sharply (blue rings in Figures 3.4[d]-[f]). This means that all the intensity peak values of the atomic columns tend to decrease, which is consistent with the corresponding intensity peak profiles. Thus, both these intensity profiles and distribution histograms clearly indicate that the intensity of the atomic columns diminished as the electron irradiation continued, which confirms the strong dependence of intensity on observation time.

It should also be noted that after the dark intensity of each atomic column, an intrinsic faulted loop (SF) was observed during the *in-situ* observation, then as all known that the intrinsic faulted loop is evolved from large vacancy clusters, which means that the dark image intensity in the HRTEM images might be caused by the induced vacancy clusters. Furthermore, the decrease in the atomic column intensity observed above as the irradiation time increased can also be observed, which proves that a number of atoms were removed from their original places, thereby leaving vacancies in the previously perfect columns. Noted that the analyzed video was recorded near the optimum defocus conditions and at $C_s = 0$, all columns in all the images were aligned in the [110] direction.

Therefore, there can also be inferred that the vacancies induced during the *in-situ* observations were along the [110] direction, which led to the inhomogeneous contrast indicated by red lines in Figures 3.4(b) and (c). Hence, the inhomogeneous contrast observed in the TEM images might have been caused by these electron irradiation-induced vacancy clusters.

3.2.3 Inhomogeneous contrast of HRTEM images by 200 kV AC-TEM

Since the inhomogeneous contrast observed in the TEM images was speculated that it might be caused by these electron irradiation-induced vacancy clusters in section 3.2.2. Here tried to show an evidence to verify it. For the HRTEM images, when an electron encounters a single, isolated atom, it can be scattered in several ways. As shown in Figure 3.5(a), the characteristics of the scattering process are controlled by several factors, such as the incident-electron energy and the atomic number/weight of the scattering atom. When there considers a specimen rather than a single atom, factors such as the thickness, density, crystallinity, and angle of the specimen to the incident beam also become important. For the scattering mechanism, the scattering cross section [69-70] between electron beams and atoms is usually defined as

$$\sigma = 1.62 \times 10^{-24} \left(\frac{Z}{E_0}\right)^2 cot^2 \frac{\theta}{2}, \quad (1)$$

where E_0 is the beam energy (keV), Z is the atomic number and θ is the scattering angle. Equation (1) indicates that a low-energy electron beam corresponds to a large scattering cross section, *i.e.*, a low-energy beam can lead to a great electron scattering by the atoms. The scattering cross section value depends on a few parameters, including the electron-beam energy. To demonstrate the influence of electron-beam energy on scattering cross section, as shown in Figure 3.5(b), here compared a 200-keV low-energy

electron beam and a 1,000-keV high-energy beam, the scattering cross section value was higher for the low-energy beam (200 keV), thereby confirming that low-energy electrons are more likely to be scattered by sample atoms than high-energy ones (1000 keV). In present experimental case, the Al atoms were knocked on by 200 kV low-energy electron beam, it means that a clear image contrast caused by point defects can be visualized.

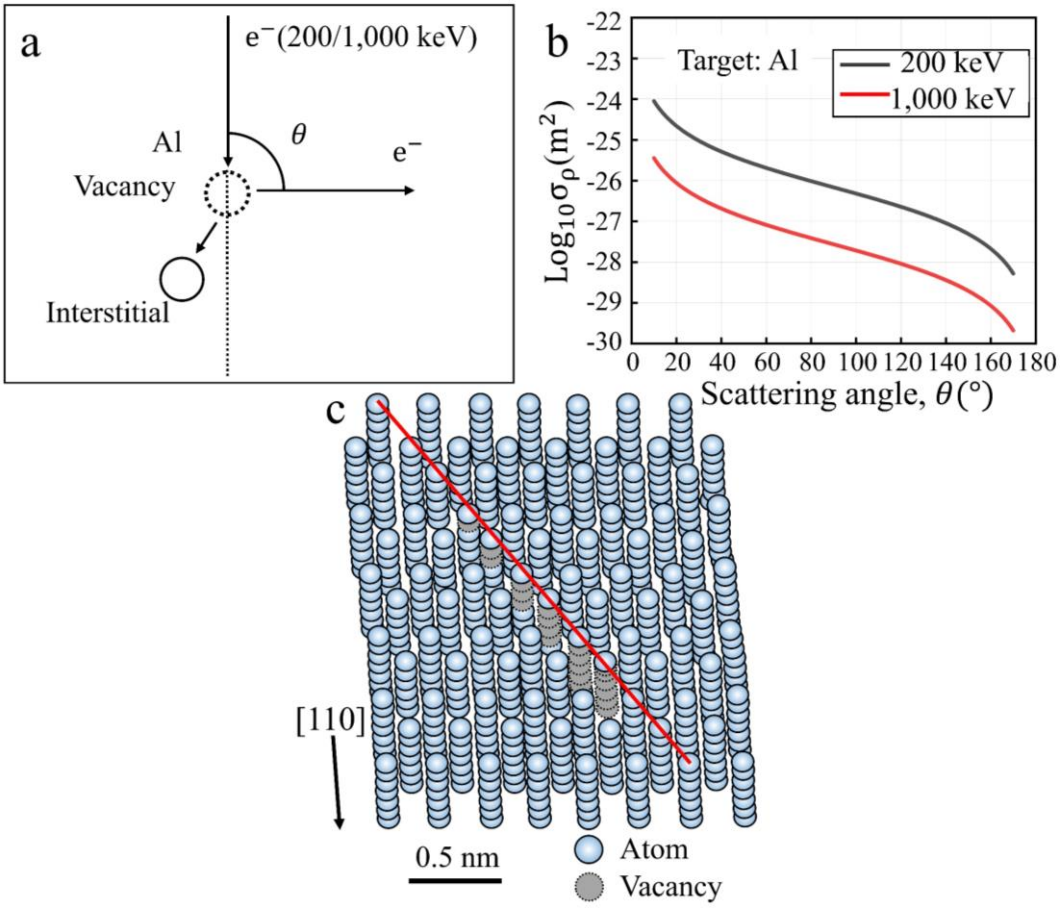

Figure 3.5 .Scattering effects during transmission electron microscopy. (a) Interaction between an incident electron and an atom of the Al sample. (b) Corresponding scattering cross section at different accelerating voltages. (c) Al crystal model with a total of 21 vacancies.

In order to verify the speculation in section 3.2.2, which is the influence of vacancy clusters on the HRTEM image, here also built a crystal model with vacancies and vacancy clusters, as shown in Figure 3.5(c). Noted that the interstitial atoms are neglected because

it is diffuse faster than vacancy, there are easy to be absorbed by sink on surface, leading to a low concentration as following previous work [71]. The crystal model was realised using the CrystalKit software [72]. Along the [110] zone axis (close-packed direction in FCC lattice), a total of 21 vacancies (the vacancy number changed from 0 to 6 with the steps of 1 in each atomic column) were given and inserted into different atomic columns, as denoted along the red line in Figure 3.5(c).

It should be noted that a 200 keV electron beam has a larger probability of being scattered by the target atoms, thereby making it more sensitive to vacancies and interstitial defects. Therefore, to investigate the influence of the vacancy clusters on the HRTEM images by 200 kV AC-TEM, here simulated several HRTEM images using the built model (Figure 3.5[c]) under 200 kV AC-TEM observations. These HRTEM images were simulated based on the multislice method using MacTempas software [73]. Simulations for different vacancy numbers (model in Figure 3.5[c]) under 200 kV AC-TEM observations (with $C_s = 500\,nm$ and defocus $\Delta f = -7, -5, -3, -1, 1, 3, 5$ and 7 nm) are presented in the Figure 3.6.

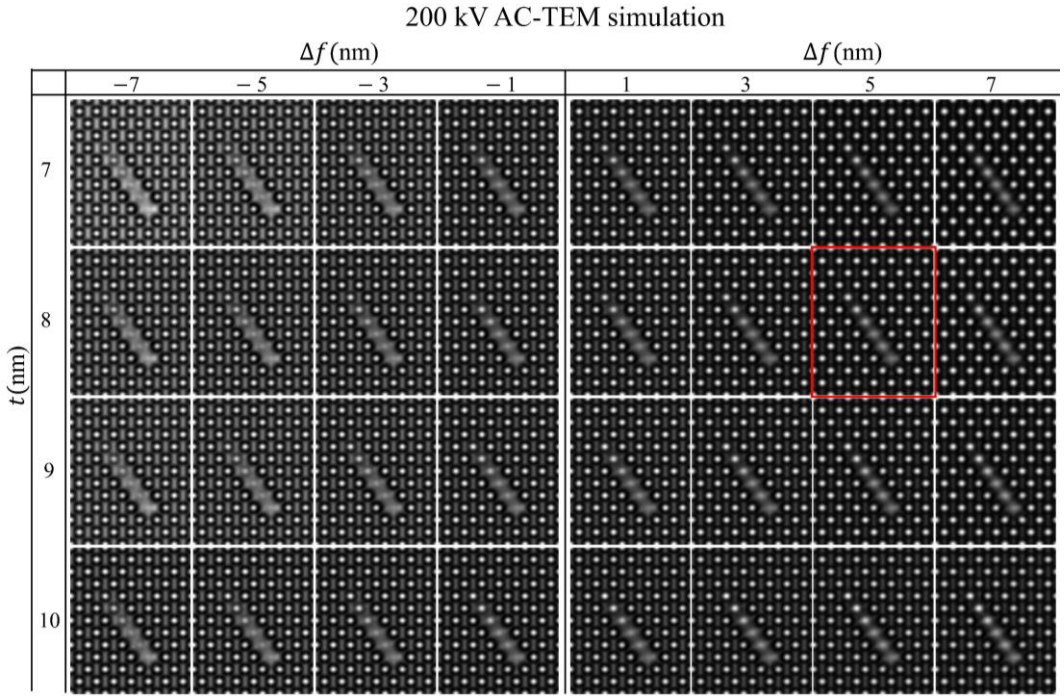

Figure 3.6. Defocus and thickness series of [110]-oriented Al crystal model simulation images using 200-kV AC-TEM. Defocus changed from −7 to 7 nm with the steps of 2 nm in the 200-kV AC-TEM images, thickness changed from 7 to 10 nm with the steps of 1 nm for this simulation.

In this simulation, in addition to the defocus, this study also varied the sample thickness ($t = 7, 8, 9$ and 10 nm) to investigate the effect of thickness on image intensity in the experimental observations using both HRTEM simulations. The simulated image contrasts for the 200 kV AC-TEM exhibited a similar clarity regardless of the defocus and thickness. Further, a high contrast of the vacancy clusters (compared with the case of no vacancy clusters) was observed, whereas almost no loss of information was observed for any defocus value. This result suggests that the 200 kV AC-TEM phase contrast imaging can reveal the vacancy defects with a small range of defocus value.

Actually, rough differences could be seen with the naked eyes in these simulated images. To reveal these differences in more detail, Figure 3.7(a) illustrates the distinct contrast images derived from one of the simulation images (red rectangle in Figure 3.6).

The intensity profiles of each atomic column (without and with vacancies) in the simulated image are displayed in Figures 3.7(b), which reveal that the intensity reduction due to the presence of vacancies was significate for the 200 kV AC-TEM, as denoted by the red lines in this image.

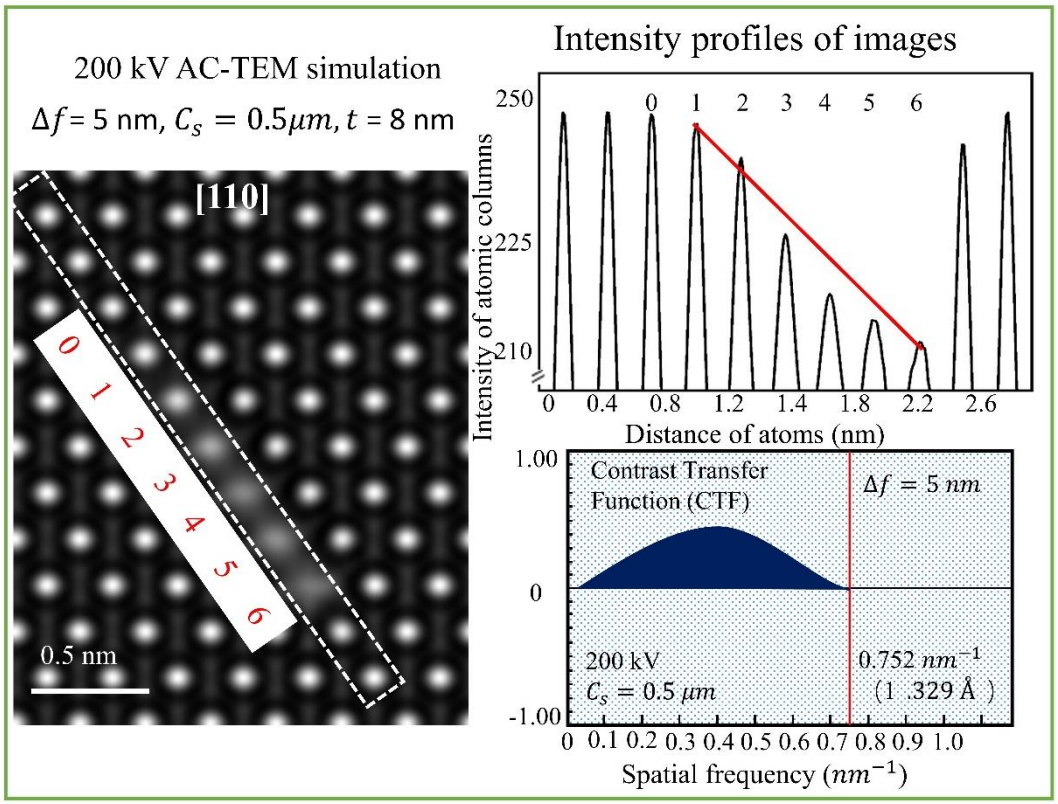

Figure 3.7. Identification of image contrast under the 200-kV AC-TEM. (a) One of simulated images from figure 3.6 and (b) the corresponding intensity peak profiles of each atomic columns of white rectangle in (a) and (c) phase contrast transfer function curves (the red lines indicate the spatial resolution).

The significant intensity reduction in the simulation image is consistent with the previous statement that the 200 kV AC-TEM is sensitive to the changing in the number of atoms in each atomic column and provides clear image contrast due to a low-energy beam. Therefore, the simulation confirmed that the vacancies and vacancy clusters appeared as clear dark image contrasts in the HRTEM images obtained by the 200 kV

AC-TEM. Meanwhile, Figure 3.7(c) presents the phase contrast transfer function (CTF) curves derived using the simulation parameters for the microscopy scenario. Note that the spatial resolution depends on the first zero point of the crossover between the transfer function (*y*-axis) and scattering vector (*x*-axis) [74] in the CTF graph. In these simulations, the spatial resolution was 0.133 nm for the 200 kV AC-TEM. The 200 kV AC-TEM phase CTF graph for the present simulation conditions had a large positive focus value, this is because that the positive focus value and with the thin specimen, the phase contrast image of the atom positions appeared in the HRTEM images as a bright contrast. Because the Al (111) interplanar spacing was 0.233 nm and considering the previously mentioned high sensitivity of 200 keV electron beams to vacancy clusters, it can be concluded that the 200 kV AC-TEM technique with high spatial resolution should be helpful when analysing Al (111) planes to obtain a good interpretable image contrast and high resolution.

3.2.4. Kinetic Monte Carlo (MC) simulation of the vacancy jumping (Appendix 1)

Although previous two sections attributed the inhomogeneous contrast shown in Figures 3.4(b) and (c) to the vacancy clusters continuously induced during the *in-situ* observation, further investigations of this interpretation of the origin of the image changes were necessary. As all known that these Al vacancies are difficult to be captured with a CCD camera given an exposure time of 0.05 s because they jump within the Al lattice with the average frequency of 50 times/frame (1,000 times in 1 s) [75]. Therefore, this study also calculated the dynamical behaviour of these jumping vacancies via a kinetic MC simulation [76-77]. For the simulation, it performed by Dr. Zhao who was a Ph.D. student of our group, and the simulated detail is shown in Appendix 1. Figure 3.8(a) displays an image snapped during the first second (20^{th} frame) of one of the simulated

videos, which shows the traces of 100 vacancy jumps at different positions in the supercell. Figure 3.8(b) illustrates the jumping trace distribution for these 100 vacancies in each atomic column position for the frame considered, which shows that each position was overlapped several times (red spheres) by the jumping of these 100 vacancies.

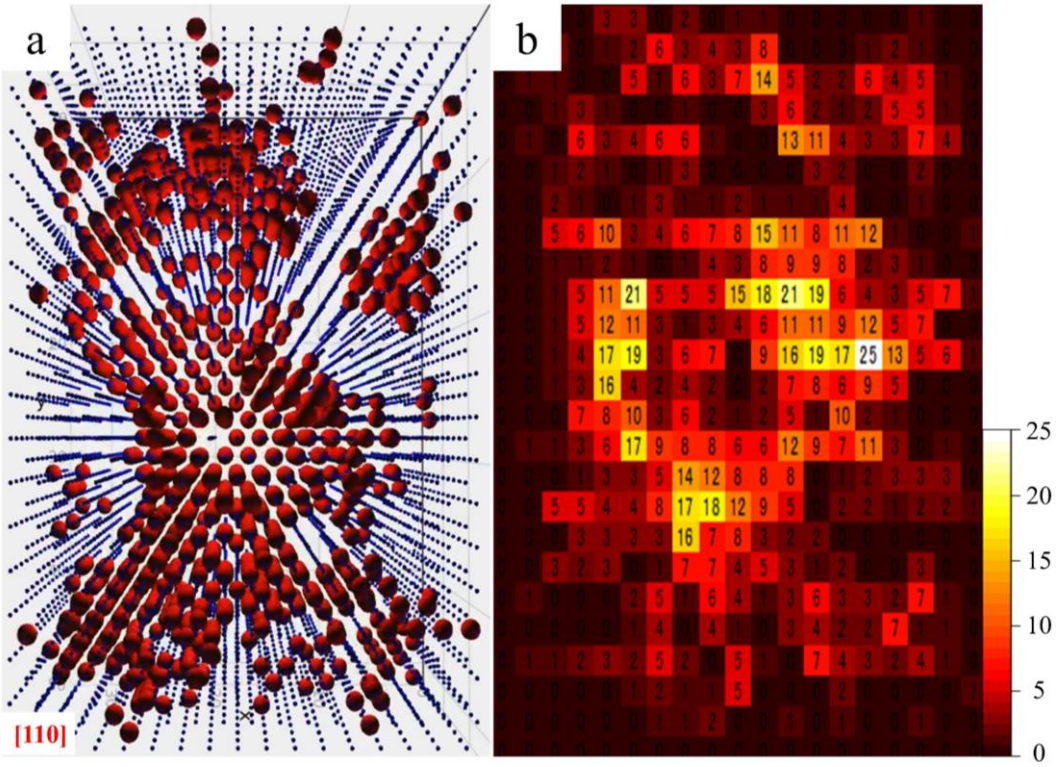

Figure 3.8. (a) Distribution of 100 vacancies in each column in 1 simulated frame. (b) Distribution of their corresponding jumping traces.

Based on the calculated MC simulation, it can further confirm that the continuous reduction of the atomic column intensities shown in Figures 3.4(2) and (3) corresponds to the induced vacancy clusters in each atomic column.

3.2.5. Disappearance of induced intrinsic SF at RT

In Sections 3.2.1-3.2.4, there described the evidence indicating that the edge dislocations at both sides of the faulted loop climb and make the growth of the faulted

loop on the (111) plane, as shown in Figures 3.3(e) and (f). And the driving force of edge dislocation migration can be considered as the electron irradiation induced vacancy migrations. Here, it proposes additional evidence for this claim. There also has an intrinsic faulted loop (SF) on the (111) plane, which revealed during an *in-situ* observation with the same usual beam flux as section 3.3.1 at RT, as shown in Figure 3.9. Note that this figure captured from video #3, which displays only the HRTEM images taken prior to and after the formation of this intrinsic faulted loop; it does not show the initial observation period (*i.e.*, when the electron beam was switched on). Meanwhile, an inhomogeneous contrast similar to that shown in Figures 3.4(b) and (c) was also observed before the faulted loop formation. Thus, it can be deduced that this faulted loop was the result of the aggregation of the electron irradiation-induced vacancy clusters during the observation.

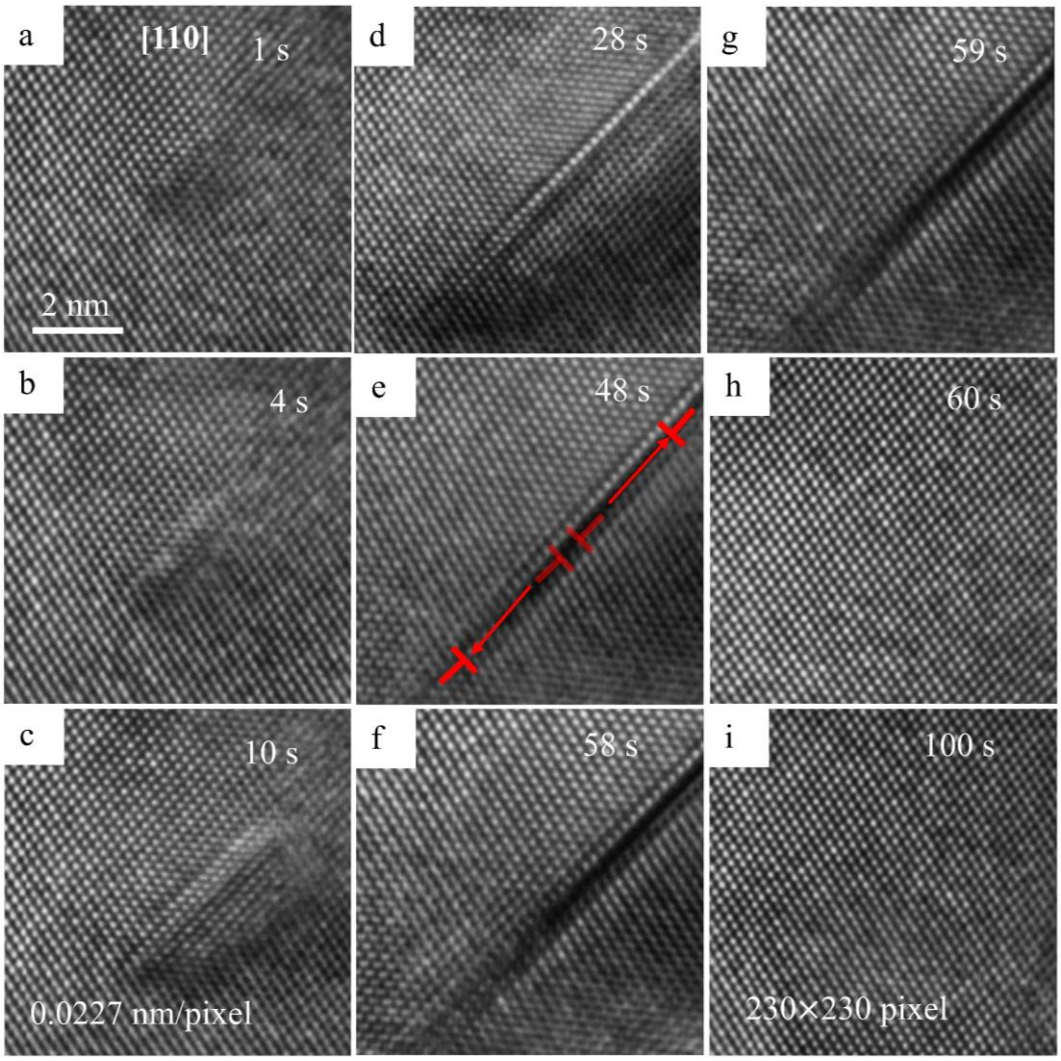

Figure 3.9. (a-i) *In-situ* HRTEM images taken at room temperature, including (a-c) the appearance of an intrinsic SF on the (111) plane, (d-f) SF growth, (g-h) SF disappearance in less than 1 frame and (i) lattice relaxation via vacancy diffusion.

It should be noted that Figure 3.9(d) shows a linear atomic layer exhibiting a brighter contrast than the other atomic layers, which has two possible interpretations. One is that most of the vacancies were absorbed by the generated faulted loop, thereby resulting in a relatively low concentration of vacancies in the surrounding area and in a bright visual contrast. The other interpretation does not consider the vacancy concentration but is instead based on the idea that when adequate vacancies aggregate into a faulted loop on

an atomic plane, the nearby atomic layer acquires a small inclination angle due to strain relaxation. By this small inclination angle satisfied the Bragg diffraction had shown brighter contrast nearby the atomic layer corresponding faulted loop.

Furthermore, the climbing process of the observed faulted loop is shown in Figures 3.9(c)-(g) and the edge dislocation marks are placed in Figure 3.9(e). The faulted loop generation and climbing processes are qualitatively similar to the section 3.3.1. Meanwhile, in 2015, Yang et al. [78] reported that such intrinsic faulted loops produced by vacancy aggregation are relatively unstable in thin samples due to a high surface energy. This is because a large surface area can act as a strong sink, which causes the faulted loop to disappear. From Figures 3.9(g) to (h), the generated faulted loop disappearing was also observed in less than 1 frame. Because SF disappearance is generally very quick (in fs), the CCD camera here used (which had an exposure time of 0.05 s) was not able to capture it, then a comprehensive illustration of the dynamic behaviour of this faulted loop disappearance cannot be identified in present study.

3.2.6 GPA mapping of faulted loop evolution process

In order to analyze the influence of point defects produced during the irradiation process on the Al thin film, the GPA method [59-61] was used to calculate the strain field surround the generated faulted loop in pure Al thin film at RT before and after the formation of faulted loop, in the irradiation process.

The strain field corresponding to the images in Figure 3.10(a)-(d) is depicted in Figure 3.10(e)-(h). It can be seen from these images that the displacement field of the Al thin film in the xy direction is generally uniform at the initial stage of irradiation (1s), as shown in Figure 3.10(a). The x and y strain components were defined as horizontal

and vertical directions along the faulted loop, as presented in Figure 3.10(a), respectively, this is because there wanted to know the strain field around the faulted loop. From this corresponded GPA result Figure 10(e), the strain field at the center (white arrow in Figure 3.10[e]) shows an inhomogeneous strain, and this strain in this local area is larger than that of in other areas. These results illustrate that early at the beginning of the irradiation, the lattice strain is concentrated in the irradiation area, that is, this area where the faulted loop will occur. In this case, this mismatched displacement in the thin Al film is given by the induced vacancies during electron irradiation and they have influence on the strain distribution in the center area with the irradiation. With the irradiation time increases, a larger strain component ε_{xy} with compression and tensile in this area was produced, there indicated that this strain field caused by an edge dislocation due to large number of vacancies, the GPA result was inserted in Figure 3.10(f).

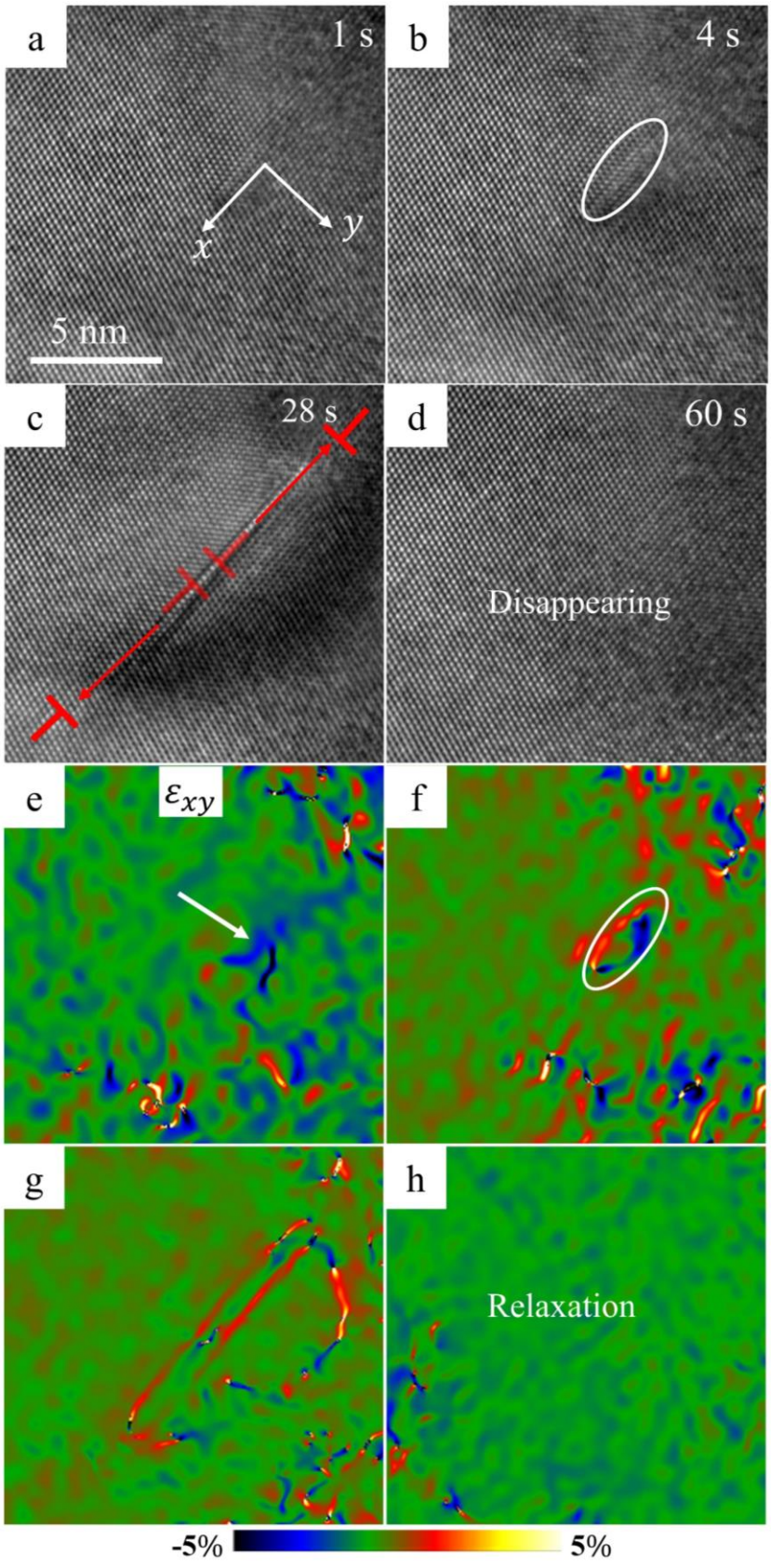
a
1 s
x
y
5 nm
b
4 s
c
28 s
d
60 s
Disappearing
e
ε_{xy}
f
g
h
Relaxation
-5%
5%

Figure 3.10. (e-f) GPA maps in a horizontal direction and vertical direction correspond to Figure 3.10(a-d).

Starting from Figures 3.10(b) to (c), a faulted loop begins to form and grow up, and the overall compression strain shows a little larger than the initial value of Figure 3.10(e), the stress increases gradually with irradiation time increasing (bright color area), and the lattice strains are mainly shown near the dislocation core, in this case, the dislocation core is the formed faulted loop. As the faulted loop grows, the lattice strain also increases with the growth of faulted loop. It is confirmed that the electron irradiation induced vacancies aggregated near the faulted loop. Afterward, Figures 3.10(c)-(d) present the process of faulted loop disappearance, from Figures 3.10(g) to (h), it is clearly to see the SF disappeared in a few seconds, and all of the edge dislocations near the faulted loop also disappeared with the faulted loop disappearing and the overall stain field shows considerable difference between the two images. This is because the strain field in the thin film easily extends close to the neighbor sinks, grain boundary or surface, then the faulted loop disappeared due to the vacancy diffusion for strain relaxation during electron irradiation. Finally, the lattice returns to an initial relaxation state after prolonged irradiation time, as shown in Figure 3.10(h). The satisfactory correspondence between experiment results and GPA maps suggests the edge dislocations at both ends of faulted loop migrate along <112> direction over the whole thickness of the specimen, then the induced faulted loop disappeared due to the strain relaxation.

3.2.7 Effect of high vacancy jumping frequency on potential contrast imaging

Temperature strongly influences the jumping frequency of vacancies and interstitial defects in the Al matrix (the higher the temperature, the faster the jumps), which may

result in different appearances in the HRTEM images. Thus, to investigate the influence of high temperatures on the inhomogeneous contrast shown in Figures 3.4(b) and (c), here compared with image contrast obtained from a same sample at 623 K. In the present study, the Al thin film prepared by electrochemical polishing, which has amorphous AlO_x layer and initial lattice defects was first *in-situ* annealed within approximately 3 min at 623 K temperature under the same beam flux as at RT to observe the variation in the image contrast. Here recorded a real-time video (video #4) for 5 min of annealing. To better show the contrast difference of the atomic columns between 623 K and RT, Figures 3.11(a)-(c) also show TEM images snapped from this video at 1, 60 and 90 s, which reveal no significant difference because the visual contrast is qualitatively similar among them. Figure 3.11(d)-(f) further display their intensity profiles. In contrast to Figures 3.4(b) and (c), here cannot see an inhomogeneous contrast caused by a lower intensity of atomic columns at 623 K.

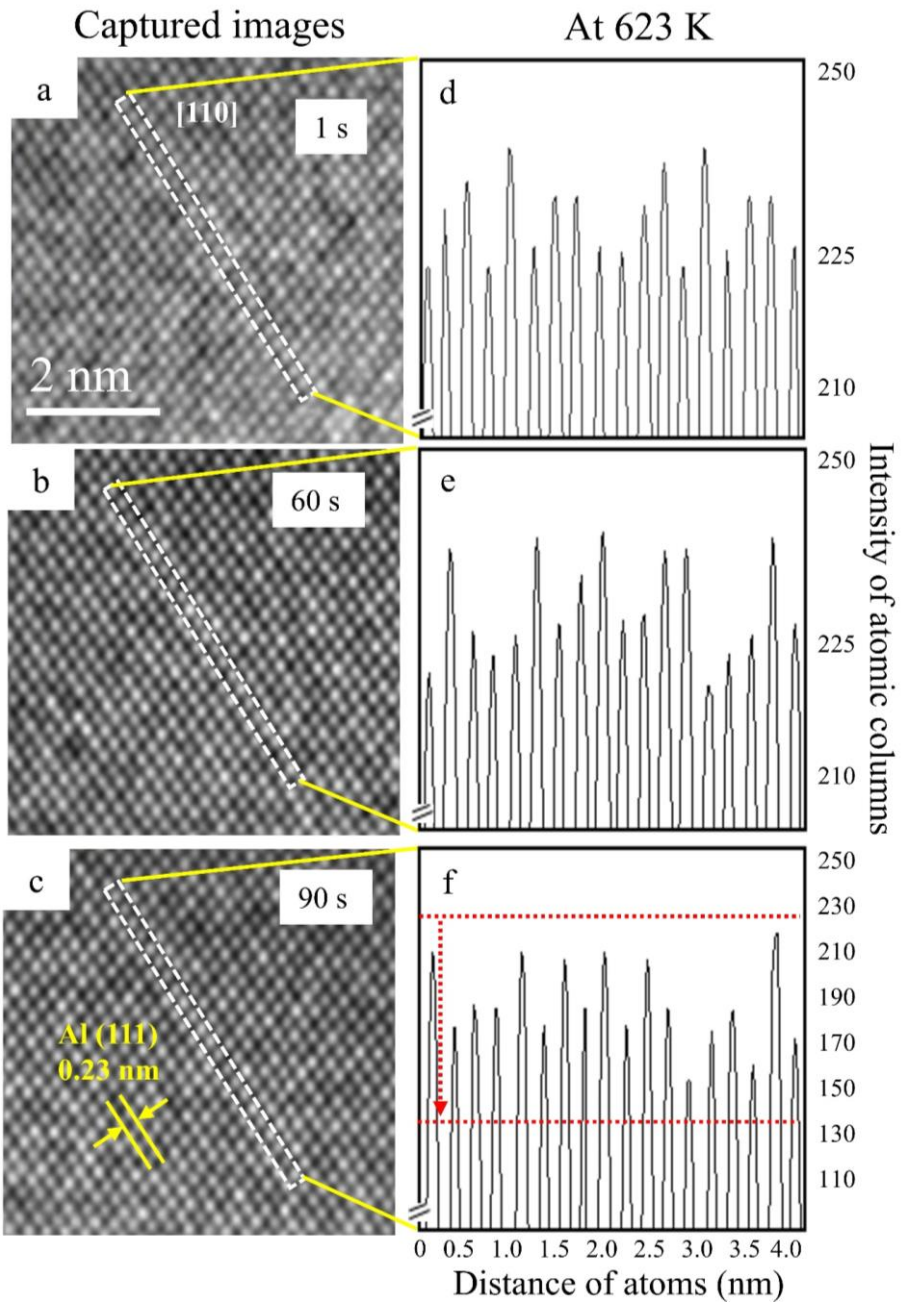

Figure 3.11. (a-c) HRTEM images taken at different times under electron irradiation at 623 K and (d-f) the corresponding intensity peak profiles of the atom columns.

Thus, from the viewpoint of the irradiation defect study, the origins of homogeneous contrast revealed in Figures 3.11(a)-(c) were tried to be distinguished from the sample preparation damages. One is that the jumping frequency of vacancies and interstitial

defects was approximately $7 \times 10^8/\mathrm{s}$ at 623 K, which is 70,000 times greater than that at RT [8]. These induced defects can be easily annihilated within the sample, thereby resulting in a lower concentration of vacancies and interstitial defects and an almost homogeneous contrast. Another factor is that the foil surface can act as a strong sink for the mobile vacancies and vacancy clusters, which tend to disappear on it. Therefore, the near homogeneous contrast observed in these HRTEM images can be attributed to a low concentration of vacancies and vacancy clusters.

3.3 Discussion

3.3.1 Induced Frank loop type in Al under electron irradiation

As describe in section 1.2, the dislocation loop type in electron irradiated pure Al is found as vacancy type and interstitial type by different researchers, and these reviews show that the nature of electron irradiation damage in Al might has major discrepancies. In present study, here surely observed the vacancy type loops, this result may be due to the sample thickness used in this study is enough thin, since the irradiation induced interstitial atoms are diffused faster than vacancy, they are easy to be absorbed by sink or surface, leading to a low concentration of interstitial atoms in the thin sample ($\geq 10\ nm$). Then, the environment of a vacancy supersaturated is obtained, and finally the vacancy type dislocation loops are easily to be produced during electron irradiation. To better show the fact, here shows schematic diagrams for a simplified understanding of the effects of interstitial atoms and vacancies on growth and shrinkage of flank loops. The sample surface and Frank loop is the sink site of point defects such as interstitial atoms and vacancies. Absorption of vacancies results in growth of the vacancy type Frank loop. If a larger number of vacancies are absorbed into the vacancy type Frank loops, the size

will be changed. Whereas this experimental phenomenon cannot be observed in thick sample due to the high concentration of interstitial atoms. These are universal theory on irradiation defects in the Al sample.

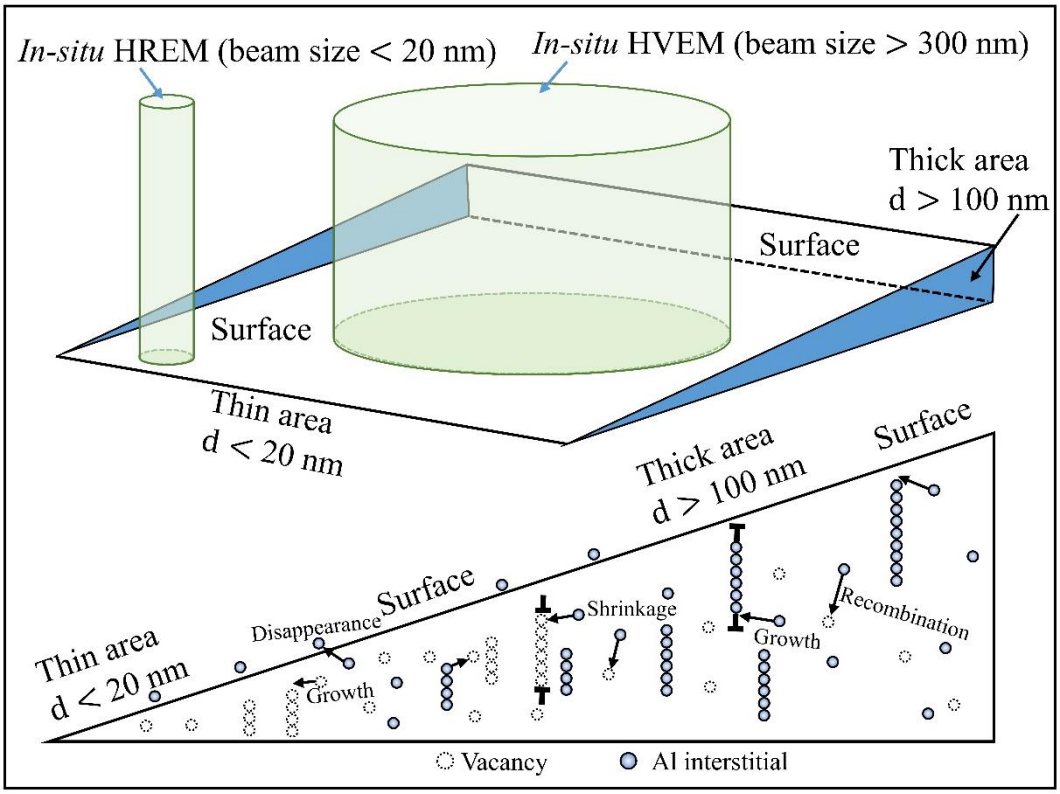

Figure 3.12. Schematic diagram of effects of interstitial and vacancy on evolutions of Frank loops.

For the observed vacancy type Frank loops in present study, another interpretation is considered the when adequate point defects were induced by a higher dose rate (0.0589 dpa/s), the interstitial atoms diffused to the sink in thin sample and the higher concentrated vacancies aggregate into a faulted loop on an atomic plane, easily. By this aggregation process had shown the vacancy type Frank loops in the atomic layer.

3.3.2 Disappearance mechanism of faulted loop in thin Al film at RT

In section 3.2.6, the disappearance mechanism of generated faulted loop was

explained by GPA results, which is due to the strain relaxation, however, this disappearance also can be explained by several mechanisms [79-83]. In this part, there also mainly considered the concept that the faulted loop disappearance can be triggered by the formation of a Shockley partial loop inside a Frank loop.

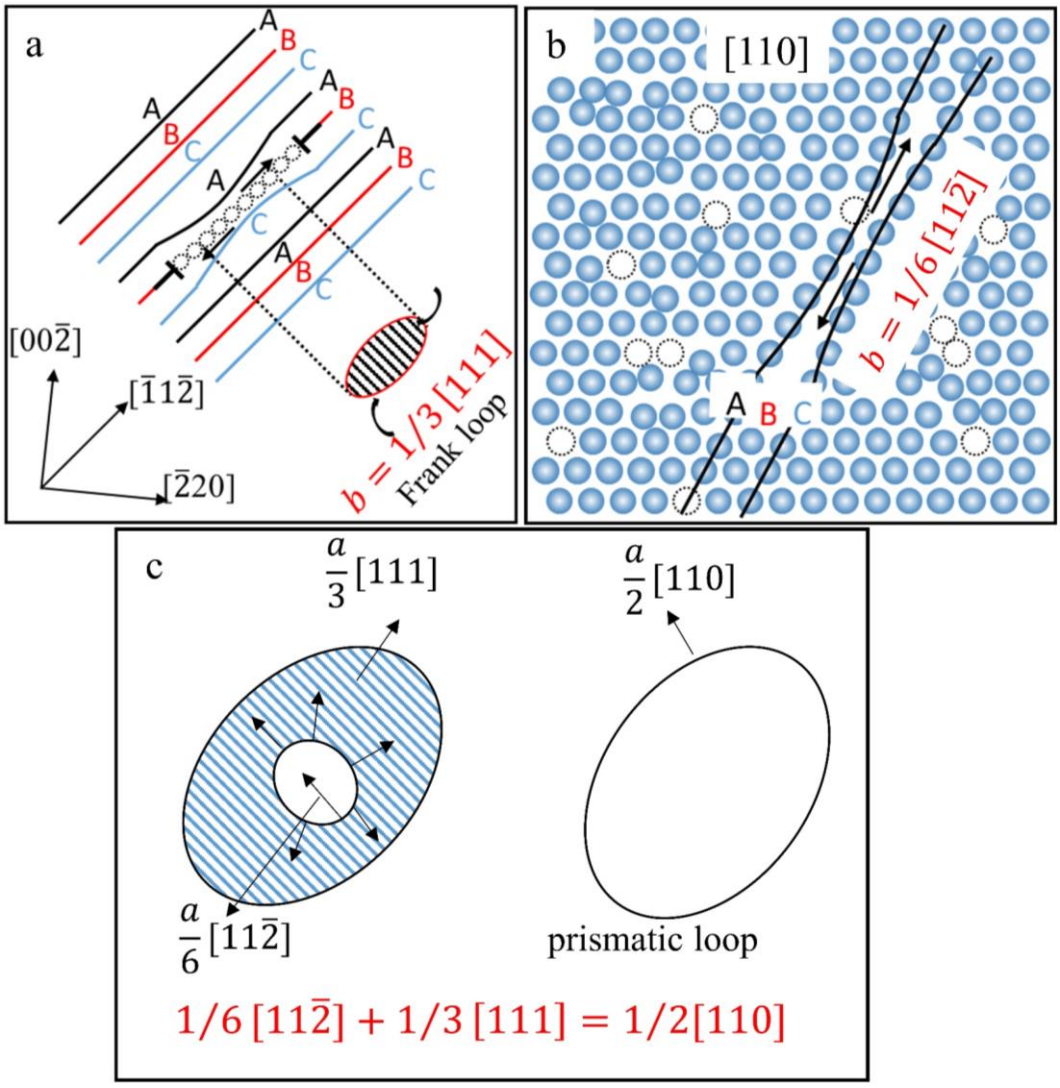

Figure 3.13. The disappearance mechanism of faulted loop in thin Al film. (a) A Frank loop in FCC lattice; (b) A Shockley partial loop caused by slippery; (c) Reaction between the Shockley partial loop and the Frank loop.

As shown in Figure 3.13, this Shockley partial loop, with $b = 1/6\,[11\bar{2}]$, reacts with the $b = 1/3\,[111]$ Frank faulted loop according to the unfaulting equation [85, 89]

$$1/6\,[11\bar{2}] + 1/3\,[111] = 1/2[110] \qquad (2)$$

Based on Eq. (2), the positive climbing of a Frank faulted loop promotes loop growth via vacancy absorption under electron irradiation. When this Frank faulted loop grows to a particular size limit, the upper layer of the Frank faulted loop slips to match the bottom layer and forms a new Shockley partial loop (Figure 3.13[b]), which then reacts with this Frank loop based on Eq. (2). The result is the production of a perfect glissile Shockley partial loop with $b = 1/2[110]$, as shown in Figure 3.13(c). Because this new dislocation loop can slip on a prismatic plane, it is also called a prismatic loop. Finally, the prismatic loop moving onto the film surface produces a slip, thereby resulting in the disappearance of the faulted loop.

3.4. Conclusion

In this study, the dynamic clustering, growth and disappearance process of dislocation loops in an FCC-Al lattice were successfully visualized during *in-situ* 200-keV electron irradiation with a beam flux of $8.61 \times 10^{20}\ e^{-} \cdot cm^{-2} \cdot s^{-1}$ at atomic-scale. Using the AC-TEM with a phase contrast and a pot-type heating holder system with an information limit of 1.5 Å, an intrinsic faulted loop (SF) with $b = 1/3\,[111]$ was formed in the (111) plane. During the *in-situ* observation, it can be able to identify the evolution of faulted loops in the acquired HRTEM images as being due to the edge dislocation migration at RT. Then, this edge dislocation loop migration, which was attributed to the point defect migration occurring during the TEM prolonged electron irradiation. Meanwhile, from the experimental observation of this faulted loop, it suggests that an inhomogeneous contrast was caused by vacancies and vacancy clusters during a prolonged observation at RT. The vacancy clustering was also discussed by HRTEM simulation and verified via a kinetic

MC simulation performed by Dr. Zhao. Subsequently, the experimental results indicated that the observed growing faulted loop was caused by the edge dislocation migration at both ends of the faulted loop, and the edge dislocation loop migration was attributed to the induced vacancy migration. Moreover, when continuing the observation, this generated faulted loop disappeared suddenly in less than 1 frame (0.05s) due to the strain relaxation. Meanwhile, here also observed a homogeneous contrast during a 5-min observation at 623 K with the same beam flux. This contrasting result occurred due to the low concentration of vacancies produced by the high jumping frequency and the instability of the vacancy cluster and faulted loop. Therefore, the experimental observation of this faulted loop confirms that the inhomogeneous contrast was caused by vacancies and vacancy clusters and that the proposed technique was able to identify it. Thus, here proposed *in-situ* HRTEM observation methods are useful in understanding the dynamical behaviour of dislocation loop at atomic-scale.

Chapter 4. Atomic scale observation of dislocation evolution in an Al-Cu alloy with coherent precipitate by *in-situ* irradiation electron microscopy

4.1 Experimental procedure

4.1.1 Material

In order to investigate the Frank loop evolution with precipitates in the coherent precipitate hardening mechanism, this study examined an Al-Cu alloy, the Al-1.7Cu (at. %) alloy (Φ3 mm × 35 mm) with a chemical composition of 98.3 at. % Al and 1.7 at. % Cu was provided by Nilaco (No. 572684). The sample fabrication of Al-Cu alloys for *in-situ* HRTEM observation were described in section 2.2 as shown in Chapter 2.

4.1.2 *In-situ* HRTEM observation

The experimental equipment used for *in-situ* observation is same as previous investigation for Al thin films, as shown in Figure 2.4. Moreover, in order to describe more detail for *in-situ* observation, the temperature history for all the videos recording for *in-situ* observation from starting point also is given as Figure 4.1. Noted that the time of removing contamination process is not discussed in this figure due to the similarity of section 3.1.3, and the total recording time (video #5 + video #6) is lasting 900 s in present study. After heating experiment, the videos recording for *in-situ* observation were started.

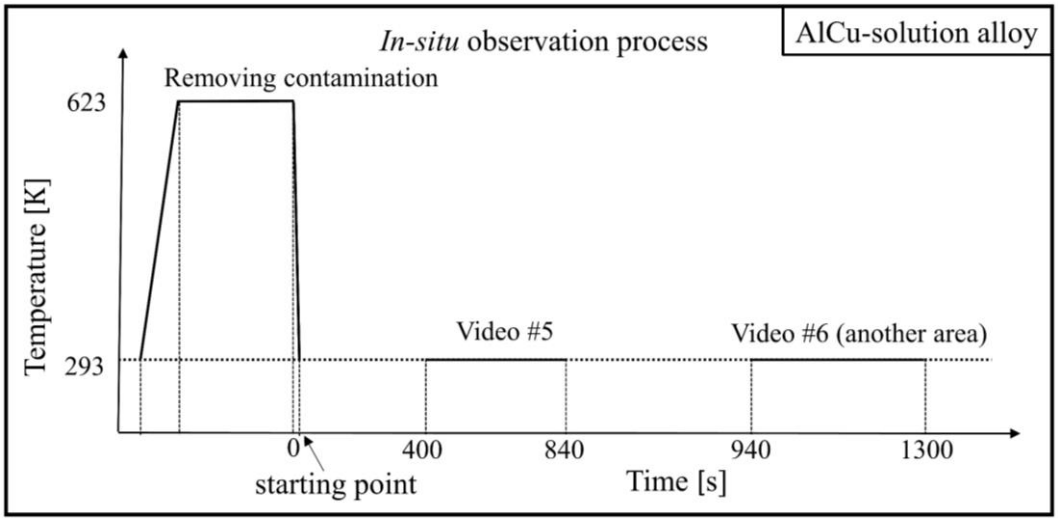

Figure 4.1. The temperature history of all the videos recording for *in-situ* observation from starting point.

4.2 Results and discussion

4.2.1 Crystal texture and chemical composition of the AlCu-solution sample

Before starting the *in-situ* electron irradiation, the initial structure and chemical composition of the AlCu-solution sample were confirmed by high-angle annular dark-field scanning-TEM (HAADF-STEM) and energy dispersive X-ray (EDX) spectroscopy, as shown in Figure 4.2. Some Cu atoms showing bright contrast (Figure 4.2[a]) in the atomic columns along the [110] zone axis of the FCC-Al lattice was observed because of their larger atomic number (Z: 29) than Al (Z: 13) [84-85], while they are invisible in the thick area, as shown in Figure 4.2(b). This means that the contrast of Cu atoms in thin area is more easily observed than thick area. Meanwhile, the contrast of the GP zone [86-88] was visible in neither thin (Figure 4.2[a]) nor thick (Figure 4.2[b]) samples. Additionally, the Cu concentration of the commercial Al-1.7Cu (at. %) alloy after dissolution treatment was calculated from the EDX spectrum with background noise subtraction to be 1.57 $\pm$ 0.02 at. %, as shown in Figure 4.2(c). The calculated Cu

concentration is lower maybe due to the inhomogeneous distribution of Cu atoms in Al-Cu alloys and a small instrumental error of the EDX calibration. Therefore, this means that Cu precipitates (including GP zones) in the AlCu-solution sample were successfully dissolved by thermal treatment at 833 K for 1 hour.

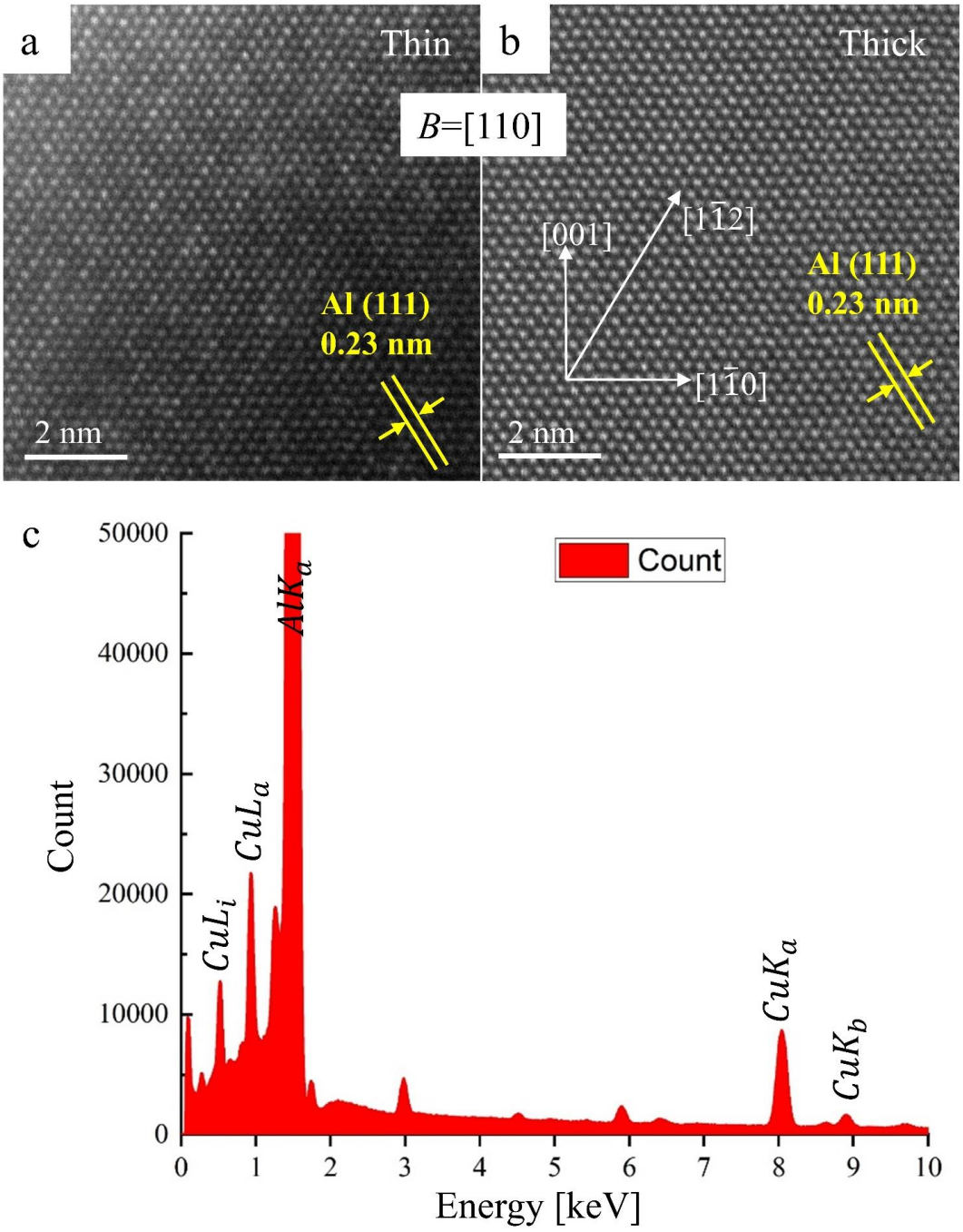

Figure 4.2. High-resolution HAADF-STEM image of the AlCu-solution sample in (a) thin and

(b) thick regions; (c) EDX spectrum of the AlCu-solution sample.

4.2.2 Evolution of dislocation loop in the Al-Cu alloy sample during *in-situ* electron irradiation HRTEM

Figures 4.3(a)-(c) show HRTEM images of the AlCu-solution sample along the $[110]$ zone axis captured from a video file at 62, 124 and 248 s, corresponding to a total irradiation time of 462, 524 and 648 s, respectively, from the starting point (gun valve open) of 200 keV electron irradiation at RT. The entire HRTEM observation process of the AlCu-solution sample is provided as a recorded movie, in the video #5. During the *in-situ* electron irradiation, along an electron incident direction of FCC-Al $[110]$, a Frank loop with Burgers vector of $1/3 < 111 >$ showed an 'abcababc' faulted loop (SF), was observed, as shown in the Figure 4.3(d), which is a higher magnification image (red rectangle) of Figure 4.3(c). From this image, the faulted loop was identified as the clustering of Al vacancies and growth of a Frank loop at the atomic scale, then the formed faulted loop was confirmed to be an intrinsic faulted loop (SF). Meanwhile, as pointed in chapter 3, two edge dislocations, located at both ends of the faulted loop, and they can climb along the $< 112 >$ direction.

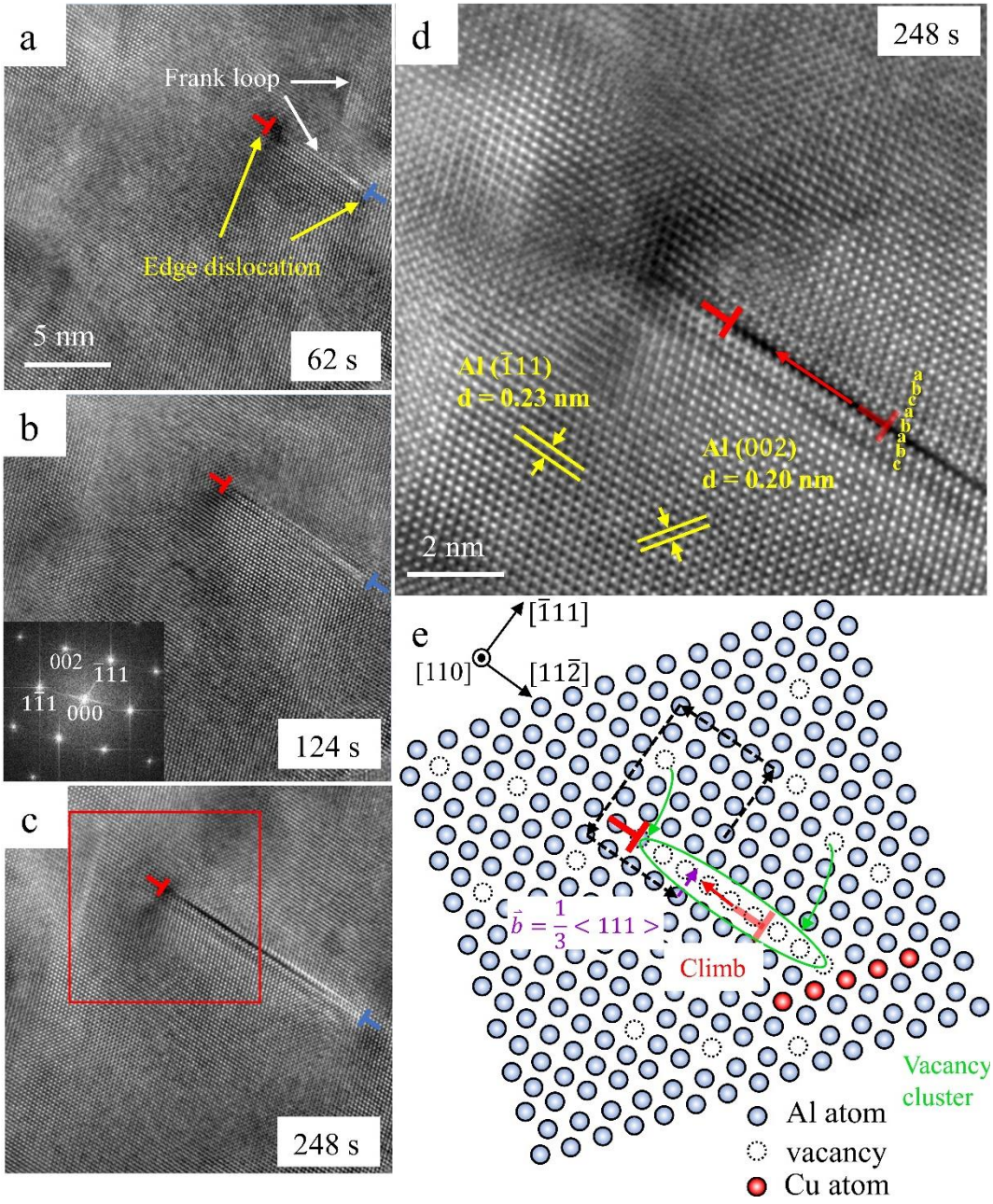

Figure 4.3. *In-situ* HRTEM images of the AlCu-solution sample taken at RT. (a-c) The appearance of edge dislocations on the (111) plane; the inserted diffraction pattern indicates that the incident beam is along the $[110]$ zone axis; (d) High magnification shows lattice spacings of d = 0.23 nm and d = 0.20 nm for Al $(\bar{1}11)$ and (002) planes; (e) Schematic diagram of the edge dislocation climbs in the AlCu-solution sample.

As shown from Figures 4.3(a) to (c), the irradiation induced vacancies tend to

aggregate and form a faulted loop, then during the irradiation process, irradiation induced more vacancies, the edge dislocation climbs and makes the growth of the faulted loop on the (111) plane. While there has an interesting finding in the Al-Cu, that is, according to the faulted loop growth process, one edge dislocation step-by-step climbed along one direction, as shown in these red edge dislocation marks in Figures 4.3(a)-(c), but the blue edge dislocation marks are stable with the irradiation time increases. Actually, a similar vacancy clustering on the $\{111\}$ plane in the pure Al lattice, also induced under electron irradiation, has been reported in previous Chapter, which is two edge dislocations located at both sides of generated faulted loop climbed along the <112> direction. However, it is noticed that a considerable difference between pure Al thin film and the present AlCu-solution sample, that is an asymmetrical climb of the edge dislocation along $[1\bar{1}2]$ direction, which is a meaningful discovery for this Al-Cu alloy. Therefore, this would be caused by the doping Cu atoms.

To understand this interesting observed result in more detail, Figure 4.3(e) is a schematic diagram describing the asymmetric climbing of the edge dislocation in the AlCu-solution sample. It can be believed that the driving force is the induced vacancy clustering on the faulted loop on $\{111\}$ planes of the FCC-Al matrix lattice. With the increased total irradiation time, a large number of vacancies migrate to the faulted loop and contribute to the asymmetric climbing of the faulted loop growth. Whereas the other side might have a stable obstacle for inhibiting the faulted loop growth, such as Cu clusters, as shown in this schematic diagram. As a result of faulted loop growth in the 20-nm-thin film, the edge dislocation stably climbed up along one of its dimensions on the $\{111\}$ planes.

Moreover, Figure 4.4(a) is a HRTEM image of the AlCu-solution sample in another

observation view field captured at 540 s after electron irradiation began (video #6). Both faulted loop *A* (6.92 nm in diameter) and faulted loop *B* (4.48) in Figure 4.4(a) were observed, and they grew to 9.38 nm and 6.92 nm, respectively, after irradiation time of 60 s. Then, in 100 s, loops *A* and *B* grew up to 10.04 and 8.49 nm, respectively. During the growth process of two faulted loops, the edge dislocations on one side of them, indicated by the red marks in Figures 4.4(a)-(c), had climbed step by step along a single direction. Whereas the edge dislocations on the other side (in blue marks) were stabilized and never climbed.

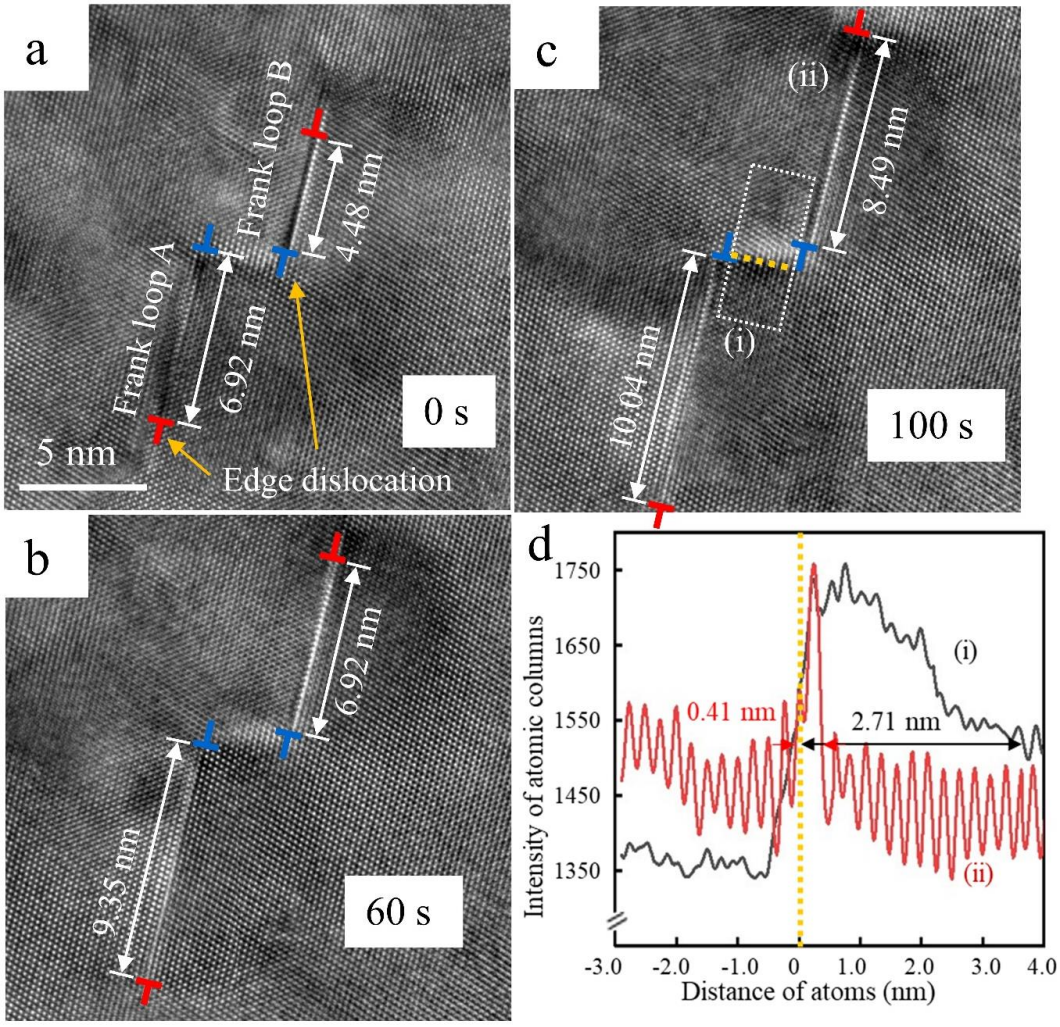

Figure 4.4. (a-c) HRTEM images of the AlCu-solution sample captured at different times under

electron irradiation at RT; (d) Intensity line profiles obtained from regions (i) and (ii) in Figure 4.4(c).

Furthermore, in this present study, a considerable strain contrast was observed between the two stable blue edge dislocations, indicated by arrows as (i) in Figure 4.4(c). The strain contrast is maintained through the growth process of two Frank loops. In addition, the distance of two faulted loops is ~2.87 nm on the {111} plane, and the HRTEM interference pattern in region (i) always suggested coherent crystal orientation with the [110] in the Al-Cu alloy lattice. Figure 4(d) shows the intensity line profiles obtained from regions (i) and (ii) in Fig. 4(c). The maximum intensity of profile (i) was almost same as that of profile (ii), and their peak widths were 0.41 nm and 2.71 nm, respectively, which implies that the peak width of profile (i) was 6.6 times larger than that of profile (ii). These results indicate that there is a coherent object experiencing a large lattice strain in region (i), which provides a stronger strain contrast than the 1/3<111> type partial dislocation. Here, one reasonable explanation is the coherent precipitates on {100}, such as the GP zones. Therefore, the coherent Cu precipitates can explain as the strain contrast, and they stopped the evolution of the faulted loops in the experimental HRTEM images during *in-situ* electron irradiation of the AlCu-solution sample.

4.2.3 GPA mapping of evolution process of faulted loops in Al-Cu alloys

In the last part of section 4.2.2, a coherent object experiencing huge lattice strain between two stable faulted loops provides a stronger strain contrast than the matrix, which was explained as the coherent precipitates on {100}, such as GP I zone. As all known that coherent precipitates and associated strain fields are of considerable importance in affecting the hardness of mentals, since their lattice strain can inhibit the edge dislocation

movement in the early stage of hardening. Therefore, the GPA method used in section 3.2.6 is also applied to measurement of displacement fields around two faulted loops in this Al-Cu alloys. Figure 4.5 presents the GPA results of Al-Cu alloys, Figures 4.5(b) shows the corresponding GPA results of Figures 4.5(a) with strain components ε_{xy}, noted that the x and y strain components were defined as horizontal and vertical directions along the faulted loop, as shown in Figure 4.5(a). It appears that a stronger strain contrast than two Frank loops can be observed in Figure 4.5(b) (white circle), which means that the coherent area provides a large lattice strain field between two Frank loops. Meanwhile, as described in section 4.2.2, this strain contrast maintains through growth process of Frank loops, so, these results indicated that there is a coherent precipitate, which gives stronger strain contrast than other area. Here explained as GP zones, a schematic is shown in Figure 4.5(c). From this schematic, the bonding length of Cu-Al atoms is much longer than the 0.286 nm bonding length of Al-Al as the smaller size of Cu atoms, as written in Figure 4.5(c).

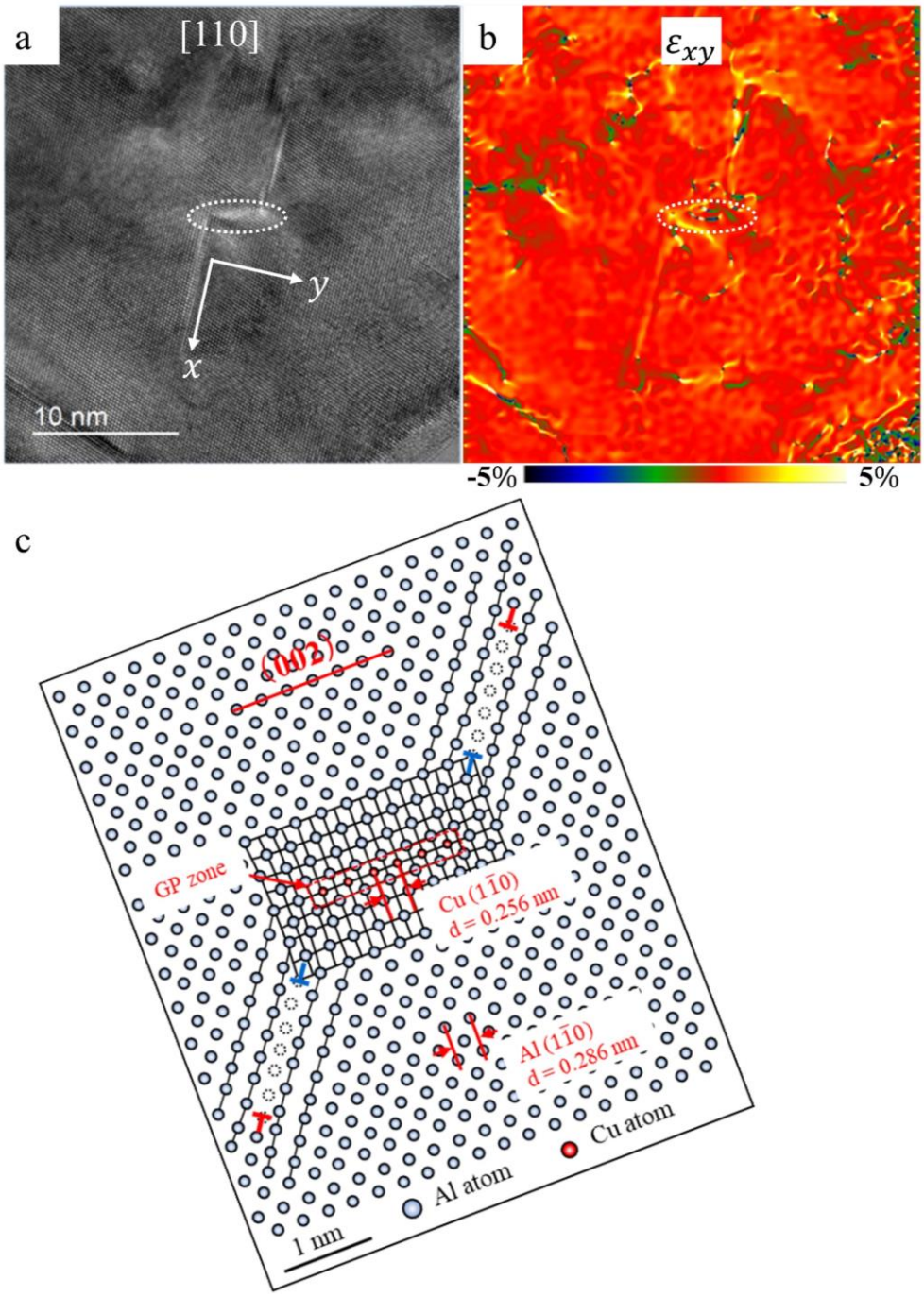

Figure 4.5. (a) A HRTEM image of the AlCu-solution sample captured at 60 s under electron irradiation at RT; (b) GPA map in a horizontal direction and vertical direction corresponded to (a); (c) Schematic image showing coherent Cu precipitate sandwiched between two Frank loops.

4.2.4 MD simulation of dislocation pinning at coherent precipitates (Appendix 2)

In section 4.2.2, the planar Cu precipitates (GP I zones: coherent) synthesised during *in-situ* electron irradiation were suggested as obstacles on {100} planes for {111} edge dislocation movement. Therefore, to investigate the interaction between GP I zones and edge dislocations during electron irradiation, there calculated the dynamical behaviour of the interaction via MD simulation performed by Prof. Suzudo from Japan atomic energy agency (JAEA). For the MD simulation, the detail is shown in Appendix 2.

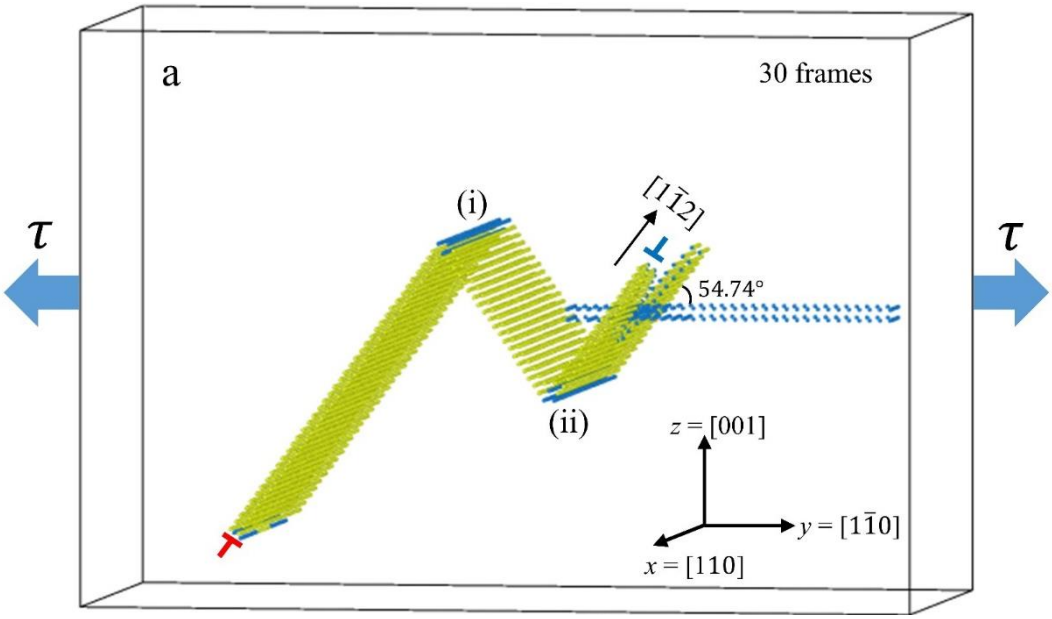

Figure 4.6. MD simulation results of the interaction between dislocations and a GP I zone, a snapshot of one of key moments of the simulation.

Here is a simple description for the simulation, from the Figure 4.6, the synthesis and growth of two edge dislocations $(\bar{1}11)$ planes, at both sides (i) and (ii) of the faulted loop, can be observed. One edge dislocation at side (i) is climbing along $[\bar{1}1\bar{2}]$ and the other reached the GP I zone with a relative angle of 54.74°, as displayed in Figure 4.6(a), showing considerable interaction. Based on the simulation, it can further confirm that the present calculated MD simulation successfully defined the coherent Cu precipitate on (001) as having the shorter bonding length of 0.132 nm working as an obstacle to the

climb of the $(11\bar{1})$ edge dislocation by the repulsive force between strain fields. This finding can be extended to GP zones on the crystallographically equivalent (100) and (010) planes, so the present inhibition effect of the strain field of coherent precipitates can be applied to actual Al-Cu alloys.

4.3 Conclusions

The dynamical behaviour of vacancy type Frank loop evolutions in an Al-1.7Cu (at. %) alloy at atomic scale has been identified by *in-situ* electron irradiation HRTEM.

In conclusion, the following findings are emphasised:

1. The formation of $a/3[111]$ intrinsic Frank loops was observed *in-situ* during electron irradiation in dissolved Al-Cu alloy and this induced an asymmetrical climb of the edge dislocation.
2. The asymmetrical climb growth of produced faulted loops during a prolonged irradiation time suggested that it might be dominated by electron irradiation induced Cu coherent precipitates.
3. By comparing the results between pure Al thin film and Al-Cu alloys, the stable Frank loops in Al-Cu alloys are observed during prolonged electron irradiation, which suggested that it can be attributed to the doping Cu atoms.
4. As a result of the different sizes of Al and Cu atoms, the lattice distortion between Cu coherent precipitates and the FCC matrix, namely strain field, inhibits dislocation climb or dislocation slip.

Chapter 5. Summary

In this study, *in-situ* HRTEM observation with electron irradiation was examined by 200 keV AC-TEM for visualizing the evolution of dislocation loops in pure Al thin film and Al-Cu alloys. The following conclusions were obtained:

From the evolution of dislocation loops in pure Al thin film during electron irradiation in Chapter 3:

1. The formation process of vacancy type faulted loops (stacking faults) in Al thin film, are clearly observed by 200 keV AC-TEM under *in-situ* electron irradiation at the atomic-scale at RT.
2. An inhomogeneous contrast before faulted loop formation was observed during *in-situ* observation, it is speculated as the electron irradiation induced Al vacancy clusters and was verified by kinetic Monte Carlo simulation method.
3. A growth process of the induced faulted loops was identified as due to the edge dislocation movements, which caused by irradiation induced vacancies and interstitial atoms migrations.
4. Then, the induced faulted loops disappeared in less 1 frame during prolonged irradiation time, the GPA results suggested that it might be due to vacancy diffusion for strain relaxation.

From the evolution of dislocation loops in Al-Cu alloys during electron irradiation in Chapter 4:

1. A formation of a/3[111] intrinsic Frank loops is also *in-situ* observed under electron irradiation in dissolved Al-Cu alloys.
2. The formed Frank loop shows an asymmetrical climb of the edge dislocation at one side of itself during a prolonged irradiation time.
3. By comparing the results between pure Al thin film and Al-Cu alloys, the stable Frank loops in Al-Cu alloys were observed during prolonged electron irradiation. It can be attributed to the effect of inhibiting of the electron irradiation induced Cu clusters.

4. By considering the result of the different sizes of Al and Cu atoms, the lattice distortion between Cu coherent precipitates and the FCC-Al matrix, namely strain field, inhibits the dislocation climb or dislocation slip.

Appendix 1

Kinetic MC simulation of the vacancy jump (in Chapter 3)

The MC simulation model is based on the residence time algorithm [89] and performed by Dr. Zhao from Tohoku university. For the simulation, an Al supercell oriented in the [110] direction was considered, which was identified from the experimental HRTEM images and diffraction patterns. The supercell size (*x*- and *y*- direction lengths) was the same as the captured observation field of view (the captured image size of Figure 3.4) for the Al thin film. As all known that the Al vacancies jumped within a limited area in the sample, which could be considered as the maximum jumping range of the vacancy. However, the potential that they would jump outside the field of view and thus be invisible to observers was present. In the simulation, to have the vacancy jumps occur only within this field of view, a single vacancy in the centre of the supercell was set, which had different thicknesses (*i.e.*, *z*-direction lengths = 1.7 and 10 nm, corresponding to 6 and 34 layer atoms, respectively), and considered its initial position coordinate as (000). And the jump frequency of this vacancy as 50 times/frame was also set, which was identical to the experimentally observed jump frequency. To ensure the simulation was statistically significant, the jumping process was cycled 1,000 times, thereby resulting in 1,000 frames (50 s). Each cycle was run again when the vacancy in the previous cycle jumped out to the simulation box in the *x, y* or *z* directions, and each jump was stochastic.

Two simulation videos (one for each supercell thickness) were obtained (video #A1 and #A2). Figures A1.1(a) and (b) compare images taken from these two videos. Both images show the traces of vacancy jumping within the crystal during 1 frame (0.05 s). The range of the traces can be considered as the jumping trace projection. Along the *x* and *y* directions, the range significantly differed depending on the supercell thickness, and it

was much smaller in the thinner supercell. For further investigation, Figures A1.1(c) and (d) display the corresponding jumping trace maps within 1 frame using the Al lattice models, which reveal the jumping ranges of approximately 0.17 and 8.35 nm^2 in the 1.7 and 10 nm-thick supercells, respectively, as indicated by the red circles in the images. This difference indicates that the jumping range strongly depends on the supercell thickness. As the sample thickness used in this study was thinner than 10 nm, the jumping range should have been below 8.35 nm^2. At the same time, the experimental observation field of view used here was approximately 20.94 nm^2, which was larger than the simulated jumping ranges of single vacancy.

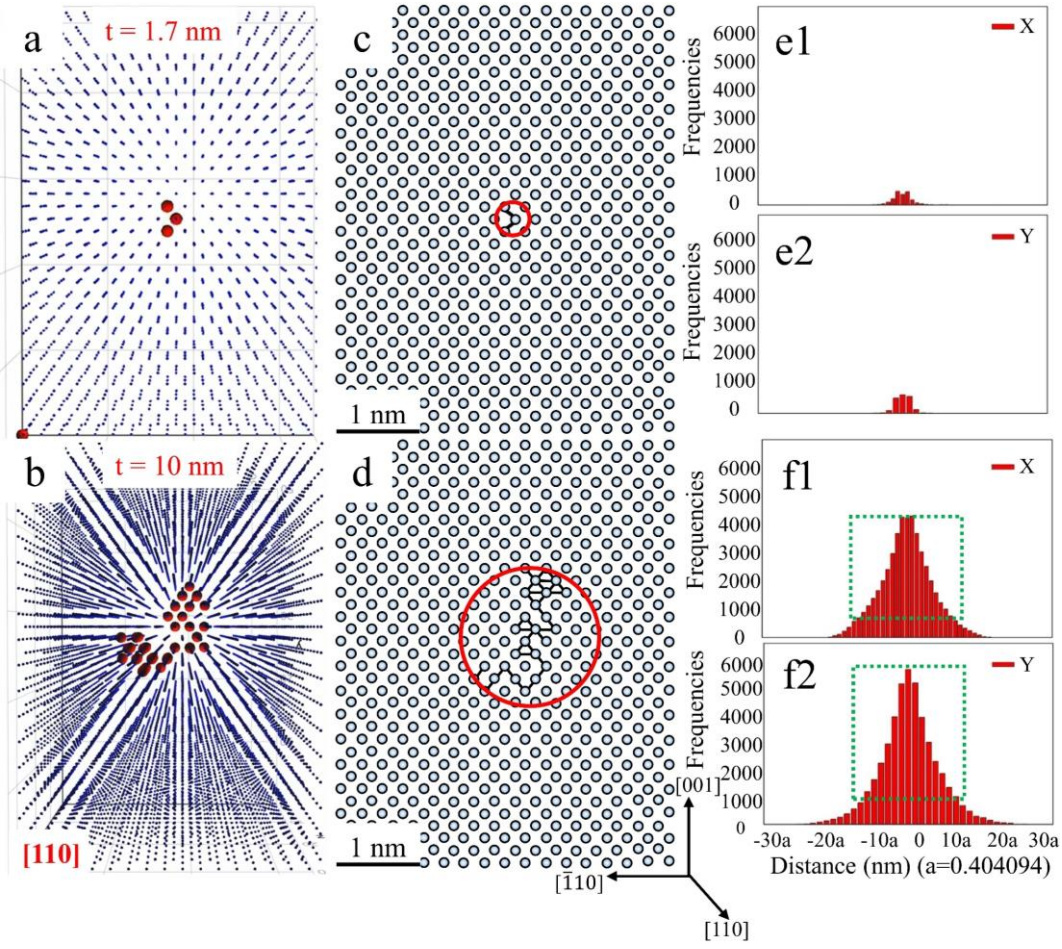

Figure A1.1. Simulation results for a single vacancy jump during 1 frame (0.05 s) in a supercell

with different thicknesses (*t*). (a, b) Images snapped from the simulation videos within 1 frame and (c, d) the corresponding jumping trace maps along with (e, f) the distance distribution between the initial and final positions along the *x* and *y* directions.

To determine the possible distribution of this vacancy jumping, the present study simulated the jumping distances between the initial and final position over 50 s (1,000 frames) for both supercell thicknesses, the results are shown in Figures A1.1(e1)-(f2). The resulting Gaussian distributions observed for both the *x* and *y* directions indicated that the electron irradiation-induced vacancies always jumped within a certain range. However, the height (frequency) of these Gaussian curves significantly differed depending on the supercell thickness, *i.e.*, the appearance of the frequency of the vacancy within a certain range was much low in the thin supercell than that of thick. This result occurred due to the vacancy more easily jumping outside the supercell in this case. These results indicate that the vacancy jumping probability within a certain range strongly depends on the supercell thickness: the thicker the supercell, the higher the appearance probability. This simulation also provided an acceptable outcome: in these experimental observations, the electron irradiation-induced vacancies appeared within a certain range and were almost confined within the matrix.

To ensure the simulation conditions consistent with the experimental ones, this study conducted an additional MC simulation. In the experiment, the irradiation rate was 0.0589 dpa/s, implying that approximately 100 vacancies were produced when capturing images at 1 s (as shown in Figure 3.4[a]). In this successive MC simulation, a supercell with 100 randomly distributed vacancies was considered. The jumping parameters were the same as those used to simulate the videos presented in the videos #A1 and #A2. The resulting dynamical simulation video is presented in the video #A3. To ensure consistency with the

experimental results shown in Figure 3.4(a), Figure A1.2(a) displays an image snapped during the first second (20th frame) of this video, which shows the traces of 100 vacancy jumps at different positions in the supercell.

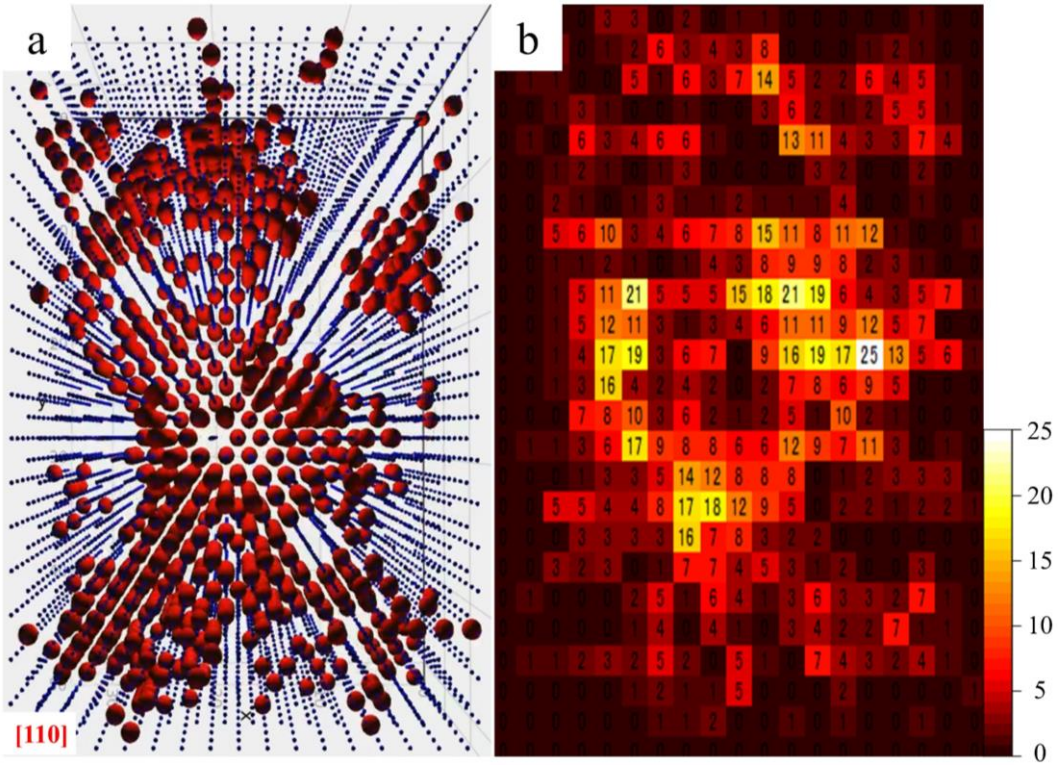

Figure A1.2. (a) Distribution of 100 vacancies in each column in 1 simulated frame. (b) Distribution of their corresponding jumping traces.

The observed overlapped traces could reveal where the jumping possibility was higher. To further investigate this, Figure A1.2(b) illustrates the jumping trace distribution for these 100 vacancies in each atomic column position for the frame considered, which shows that each position was overlapped several times (red spheres) by the jumping of these 100 vacancies. Each position reported an overlapping value, which indicated the appearance times of the vacancies in these positions. Further, this represents the different probabilities (different numbers of red spheres) of these vacancies jumping to different positions. A high jumping time value signifies a high probability that the vacancies would

jump onto these positions, and vice versa. Further, the different colours shown in Figure A1.2(b) indicate different vacancy appearance times: the brighter the colour, namely the larger the value, the greater the appearance time. Therefore, these different colours can be translated to provide an inhomogeneous image. The abovementioned inhomogeneous contrast experimentally observed in the HRTEM images might have been a result of the different appearance times of the 100 vacancies in each position. From the above simulations, both the single jumping vacancy and the 100 jumping vacancies preliminarily demonstrate that the inhomogeneous contrast in the HRTEM images was caused by the induced vacancies and vacancy clusters and can be identified via the 200 kV AC-TEM.

Moreover, vacancy clusters may form where the jumping probability is high as these positions are able to aggregate more vacancies during prolonged observations, which result in the darkest contrast in the HRTEM images. The darkest and most inhomogeneous contrast observed in the experimental results, which is indicated by the red rectangle in Figure 3.4(c), can be attributed to the presence of large vacancy clusters. Based on this interpretation, it can further confirm that the continuous reduction of the atomic column intensities shown in Figures 3.4(2) and (3) corresponds to a number of vacancy clusters in atomic column.

Appendix 2

MD simulation of dislocation pinning at coherent precipitates (in Chapter 4)

In section 4.2.4, to investigate the interaction between GP I zones and edge dislocations during electron irradiation, the dynamical behaviour of the interaction was calculated via MD simulation, which performed by Prof. Suzudo from Japan atomic energy agency (JAEA). For the MD simulation, which was based on the FCC-Al lattice, one (001) GP zone and one Frank loop (SF) on the $(1\bar{1}1)$ plane were initially prepared in three-dimensional space, consisting of *x*, *y* and *z* axes of $[110]$, $[1\bar{1}0]$ and $[001]$ directions [90]. To better show the interaction process, the (001) GP zone is shown by the blue colour, and the $(1\bar{1}1)$ Frank loop as displayed by green colour is shown at the centre of the MD simulation box. The GP zones in Al-Cu alloys were considered as single-layer plates of Cu atoms with the width of 2 nm. The original size of the MD simulation box was approximately $11 \times 23 \times 16$ nm^3 and included 256,000 atoms.

To describe the climb of the edge dislocation, 0.001 tensile strain along the $[1\bar{1}0]$ direction was imposed to the MD simulation box and atomic positions in the box were relaxed. Noted that the step-wise tensile deformation was associated with step-wise compressive deformation along the *x*- and *z*-directions according to Poisson ratio of Al, *i.e.*, 0.33, Figure A1.3(a) shows a snapshot corresponding to the 30th step of the lattice relaxation as a key point of the MD simulation results.

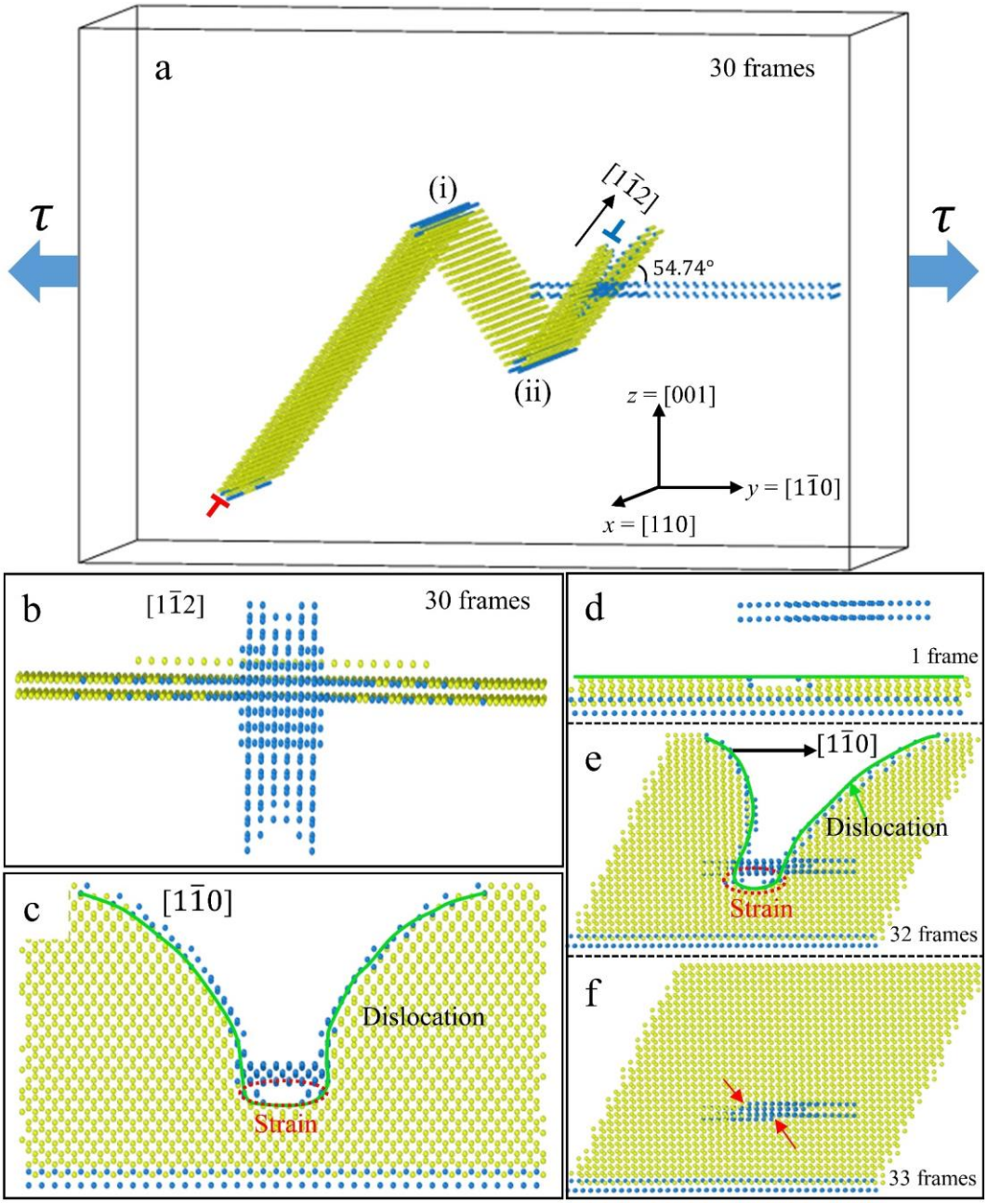

Figure A1.3. MD simulation results of the interaction between dislocations and a GP I zone. (a) Snapshot of key moments of the simulation; (b-c) Interaction regions of (a) along the [112] and [1$\bar{1}$0] directions; (d) Complete interaction process in the MD simulation. The colouring of atoms is based on common neighbour analysis method.

All steps of the lattice relaxation are presented as a video file (video #A4). In this movie, the synthesis and growth of two edge dislocations ($\bar{1}11$) planes, at both sides (i) and (ii)

of the faulted loop, can be observed. One edge dislocation at side (i) is climbing along $[\bar{1}1\bar{2}]$ and the other reached the GP I zone with a relative angle of 54.74°, as displayed in Figure A1.3(a), showing considerable interaction. Figures A1.3(b) and (c) are slice views of the MD simulation box at the crossing of the edge dislocation and GP zone along the $[1\bar{1}2]$ (video #A5) and $[1\bar{1}0]$ (video # A6) directions. The green line connecting atoms on the misfit strain field (blue spheres) can be considered as a dislocation line. It is clear to see that the dislocation line was bent significantly under the influence of the negative lattice strain field of the GP zone. The repulsive force was greatest in the red-circled area in Figure A1.3(c).

The interaction between the dislocation and strain field of the coherent precipitate is positioned at the initial stage of precipitation hardening, much earlier than the cutting-Orowan transition. As described in slice images in Figures A1.3(d)-(f) (video #A7), the lattice strain was perfectly relaxed when the GP zone was cut, and the dislocation passed through. there iterated the deformation step until the edge dislocation was unpinned from the GP-zone, where the tensile strain and stress were 0.033 and 2.27 GPa. Unfortunately, the cutting of the GP zone and relaxation of the edge dislocation happened quickly and in just one frame, which is indicated by Figures A1.3(e) and (f). Details of the cutting mechanism in the GP zone were not simulated at the atomic scale. However, the present MD simulation successfully defined the coherent Cu precipitate on (001) as having the shorter bonding length of 0.132 nm working as an obstacle to the climb of the $(11\bar{1})$ edge dislocation by the repulsive force between strain fields. This finding can be extended to GP zones on the crystallographically equivalent (100) and (010) planes. Similarly, general mixed dislocations can also be decomposed into independent edge and helical components in dislocation theory, so the present inhibition effect of the strain field of

coherent precipitates can be applied to actual Al-Cu alloys.

References

[1] S. Jumel, J.V. Duysen, J. Ruste, C. Domain, Interactions between dislocations and irradiation-induced defects in light water reactor pressure vessel steels, J. Nucl. Mater., 346 (2005), pp: 79-97.

[2] Z. Jiao, J. Hesterberg, G.S. Was, Insights into the sources of irradiation hardening in a neutron irradiated 304L stainless steel following post-irradiation annealing, J. Nucl. Mater., 526 (2019), 151754.

[3] R. Nakai, K. Yabuuchi, S. Nogami, A. Hasegawa, The effect of voids on the hardening of body-centered cubic Fe, J. Nucl. Mater., 471 (2016), pp: 233-238.

[4] K. Lu, L. Lu, S. Sureshi, Strengthening Materials by Engineering Coherent Internal Boundaries at the Nanoscale, Science, 324 (2009), pp: 349-352.

[5] M. Horiki, S. Arai, Y. Satoh, M. Kiritani, Identification of the nature of small point defect clusters in neutron irradiated Fe-16Ni-15Cr by means of electron irradiation, J. Nucl. Mater., 255 (1998), pp: 165-173.

[6] F.R. Wan, Q. Zhan, Y. Long, S.W. Yang, G.W. Zhang, Y.F. Du, Z.J. Jiao, S. Ohnuki, The behaviour of vacancy-type dislocation loops under electron irradiation in iron, J. Nucl. Mater., 455 (2014), pp: 253-257.

[7] Y. Sekio, N. Sakaguchi, Effect of Nickel Concentration on Radiation-Induced Diffusion of Point Defects in High-Nickel Fe-Cr-Ni Model Alloys during Neutron and Electron Irradiation, Mater. Trans., 60 (2019), pp: 678-687.

[8] M.J. Makin, Electron displacement damage in copper and aluminum in a high voltage electron microscope, The Philosophical magazine: A journal of theoretical experimental and applied physics, 18 (1968), pp: 637-653.

[9] M. Iphoeski, M. S. Spring, Electron radiation damage in a high voltage electron

microscope, The Philosophical magazine: A journal of theoretical experimental and applied physics, 20 (1969), pp: 937-941.

[10] M. Iphoeski, M. S. Spring, Vacancy tetrahedra in copper due to electron irradiation in the high-voltage microscope, The Philosophical magazine: A journal of theoretical experimental and applied physics, 22 (1970), pp: 1279-1283.

[11] M. Kiritani, H. Takata, K. Moriyama, F. E. Fujita, Mobility of lattice vacancies in iron, The Philosophical magazine: A journal of theoretical experimental and applied physics, 40 (1979), pp: 779-802.

[12] M. Kiritani, N. Yoshida, H. Takata, Y. Maehara, Growth of Interstitial Type Dislocation Loops and Vacancy Mobility in Electron Irradiated Metals, J. Phys. Soc. Jpn., 38 (1975), pp: 1677-1686.

[13] T. Hayashi, K. Fukumoto, H. Matsui, Effect of undersized solute atoms on point defect behaviour in V-A (A ¼ Fe, Cr and Si) binary alloys studied by using HVEM, J. Nucl. Mater., 307-311 (1998), pp: 930-934.

[14] K. Arakawa, K. Ono, H. Mori, *In-situ* Transmission Electron Microscopy of the Dynamics of Point-Defect Clusters in Metals, AIP conference proceedings, 999 (2008), pp: 66-78.

[15] T. Hamaoka, Y. Satoh, H. Matsui, One-dimensional motion of interstitial clusters in iron-based binary alloys observed using a high-voltage electron microscope, J. Nucl. Mater., 433 (2013), pp: 180-187.

[16] T. Hamaoka, Y. Satoh, H. Matsui, One-dimensional motion of self-interstitial atom clusters in A533B steel observed using a high-voltage electron microscope, J. Nucl. Mater., 399 (2010), pp: 26-31.

[17] Y. Satoh, H. Abe, T. Matsunaga, Radiation-induced glide motion of interstitial

clusters in concentrated alloys, Philosophical Magazine, 94 (2014), pp: 2170-2187.

[18] J. Gao, Y. Du, S. Ohnuki, F. Wan, Evolution of dislocation loops in annealed iron pre-irradiated with hydrogen ion in high-voltage electron microscope, J. Nucl. Mater., 481 (2016), pp: 81-87.

[19] N. Yoshida, M. Kiritani, F.E. Fujita, Electron Radiation Damage of Iron in High Voltage Electron Microscope, J. Phys. Soc. Jpn., 39 (1975), pp: 170-179.

[20] N.Yoshida, M. Kiritani, Point Defect Clusters in Electron-Irradiated Gold, J. Phys. Soc. Jpn., 35 (1973), pp: 1418-1429.

[21] M.J. Makin, Electron displacement damage in copper and aluminum in a high voltage electron microscope, The Philosophical magazine: A journal of theoretical experimental and applied physics, 18 (1968), pp: 637-653.

[22] Y.M. Platov, V.P. Kolotov V.M. Lazorenko, V.I. Tovtin , F.A. Khasanov, Nucleation and Growth of Interstitial Dislocation Loops in Irradiated Aluminum, Inorganic Materials: Applied Research, 3 (2012), pp: 183-185.

[23] K. Shiraishi, A. Hishinuma, Y. Katano, T. Taoka, Electron Irradiation Damage in Aluminum in a High Voltage Electron Microscope, J. Phys. Soc. Jpn., 32 (1972), pp: 964-971.

[24] A. Wolfenden, Damage in Aluminum by 200 kV electrons, J. Nucl. Mater., 38 (1971), pp: 114-115.

[25] A. Wolfenden, Multi-faulted dislocation loops in electron bombarded aluminum, Micron, 4 (1973), pp: 295-305.

[26] M. Kiritani, N. Yoshida, H. Takata, Interstitial Clusters in Electron Irradiated Aluminum, J. Phys. Soc. Jpn., 36 (1974), pp: 720-729.

[27] S. Jitsukawa, K. Hojou, Effect of temperature and flux change on the behavior of

radiation induced dislocation loops in pure aluminum, J. Nucl. Mater., 212 (1994), pp: 221-225.

[28] P. Rao, Report #1750, The Materials Science Center, Cornell University, Ithaca, NY (1972).

[29] W.J. Yang, R.A. Dodd, G.L. Kulcinski, Electron irradiation damage in high purity aluminum, J. Nucl. Mater., 64 (1977), pp: 157-166.

[30] K.A. Shoaib, R. L. Segall, Dependence of radiation damage on deviation from the Bragg angle, Philosophical Magazine, 180 (2006), pp: 1269-1272.

[31] G.S. Was, The displacement of atoms, Fundamentals of Radiation Materials science Metals and Alloys, second ed., Berlin Springer, 2017, pp: 77-89.

[32] N.T.H. Trung, H.S.M Phuong, M.D. Starostenkov, V.V. Romanenko, V.A. Popov, Threshold displacement energy in Ni, Al and B2 NiAl, IOP Conf. Ser. Mater. Sci. Eng., 447 (2018), 012004.

[33] A. Bourret, Irradiation damage microscope and threshold energy determination, Phys. Status. Solidi (a), 4 (1971), pp: 813-825.

[34] A. Wolfenden, Damage in aluminum by 200kV electrons, J. Nucl. Mater., 38 (1971), pp: 114-115.

[35] A. Wolfenden, Effects of preinjected hydrogen on the electron displacement damage in 1100 aluminum, J. Nucl. Mater., 40 (1971), pp: 351-352.

[36] A. Wolfenden, Electron radiation damage near the threshold energy in aluminum, Radiation Effects, 14 (1972), pp: 225-229.

[37] G. Esteban-Manzanares, E. Martnez, J. Segurado, L. Capolungo, J. LLorca, An atomistic investigation of the interaction of dislocations with Guinier-Preston zones in Al-Cu alloys, Acta Mater., 162 (2019), pp: 189-201.

[38] A.J.E. Foreman, M.J. Makin, Dislocation movement through random arrays of obstacles, Philosophical Magazine, 131 (2006), pp: 911-924.

[39] D.J. Bacon, U.F. Kocks, R.O. Scattergood, The effect of dislocation self-interaction on the Orowan stress, Philosophical Magazine, 6 (2006), pp: 1241-1263.

[40] R.O. Scattergood, The strengthening effect of voids, Acta Mater., 30 (1982), pp: 1665-1677.

[41] Y.N. Osetsky, D.J. Bacon, Void and precipitate strengthening in a-iron: what can we learn from atomic-level modelling, J. Nucl. Mater., 323 (2003), pp: 268-280.

[42] B.D. Wirth, V.V. Bulatov, T.D. Rubia, Dislocation-Stacking Fault Tetrahedron Interactions in Cu, J. Eng. Mater. Technol., 124 (2002), pp: 329-334.

[43] R.B. Nicholson, J. Nutting, Direct observation of the strain field produced by coherent precipitated particles in an age-hardened alloy, The Philosophical magazine: A journal of theoretical experimental and applied physics, 29 (2006), pp: 531-535.

[44] Z.A. Guenechea, S.E. Offerman, Substitution Case Study: Replacing Niobium by Vanadium in Nano-Steels, World Scientific Series in Current Energy Issues, Critical Materials (2019) pp: 193-221.

[45] M. Charleux, F. Livet, F. Bley, F. Louchet, Y. Bréchet, Thermal ageing of an Fe–Cu alloy: Microstructural evolution and precipitation hardening, The Philosophical magazine A, 4 (2006), pp: 883-897.

[46] T. Nagase., P.D. Rack., J.H. Noh., T. Egami, *In-situ* TEM observation of structural changes in nano-crystalline CoCrCuFeNi multicomponent high-entropy alloy (HEA) under fast electron irradiation by high voltage electron microscopy (HVEM), Intermetallics, 59 (2015), pp: 32-42.

[47] K. Yoshida, T. Kawasaki, A. Kuwabara, Y. Ukyo, Y. Ikuhara, *In-situ* electron

microscopic observation of electrochemical Li-intercalation into MoS2, Solid State Ion, 357 (2020), 115488.

[48] P.P. Liu, S.N. Jiang, Y.F. Du, Q. Zhan, H.F. Zhao, W.T. Han, X.O. Yi, S. Ohnuki, F.R. Wan, Point defect mobility in hydrogen pre-implanted vanadium under electron irradiation, Mater. Charact., 174 (2021), 111014.

[49] K.F. Hale, M. Henderson-Brown, Y. lshida, Proc. 5th European Congress on Electron Microscopy, 1972, pp: 350.

[50] M. Shimotomori and R.R. Hasiguti, J. Japan Inst. Met., (43)1979, pp: 4.

[51] D. Caillard, S.L. Martin, Acta Metall., (31) 1983, pp: 813.

[52] https://myscope.training/myscope/images/tem/schematic.png.

[53] O. Scherzer, The theoretical resolution limit of the electron microscope, J. Appl. Phy., 20 (1949), pp: 20-29.

[54] M. Haider, H. Rose, S. Uhlemann, E. Schwan, B. Kabius, K. Urban, Electron microscopy image enhanced, Nature, 392 (1998), pp: 768-769.

[55] H. Rose, Aberration correction in electron microscopy, Int. J. Mater. Res., 97 (2016), pp: 44-48.

[56] K.W. Urban, Studying Atomic Structures by Aberration-Corrected Transmission Electron Microscopy, Science, 321 (2008), pp: 506-510.

[57] M.A. O'Keefe, L.F. Allard, D.A. Blom, HRTEM imaging of atoms at sub-Angstrom resolution, J. Electron Microsc., 54 (2005), pp: 169-180.

[58] Y. Shimada, K. Yoshida, K. Inoue, T. Shiraishi, T. Kiguchi, Y. Nagai, T.J. Konno, Evaluation of spatial and temporal resolution on *in-situ* annealing aberration-corrected transmission electron microscopy with proportional-integral-differential controller, Microscopy, 68 (2019), pp: 271-278.

[59] https://www.hremresearch.com/ja/gpa/.

[60] M.J. Hytch, E. Snoeck, R. Kilaas, Quantitative measurement of displacement and strain fields from HREM micrographs, Ultramicroscopy, 74 (1998), pp:131-146.

[61] M.J. Hytch, Mapping stress and strain in nanostructures by high-resolution transmission electron microscopy, Microelectronic Engineering, 84 (2007), pp: 460-463.

[62] https://www.hremresearch.com/.

[63] M.J. Hytch, J. Putaux, J. Penisson, Measurement of the displacement field of dislocations to 0.03 Å by electron microscopy, Nature, 423 (2003), pp: 270-273.

[64] D. Wu, H. Xie, X. Dai, R. Wang, A novel method to fabricate micro-gratings applied for deformation measurement around a crack in a thin film, Meas. Sci. Technol., 25 (2014), 025012.

[65] Q. Wang, H. Xie, Z. Liu, X. Lou, J. Wang, K. Xu, Z. Zhang, J. Liao, C. Gu, Residual stress assessment of interconnects by slot milling with FIB and geometric phase analysis, Opt. Laser Technol. 48 (2010), pp: 1113-1118.

[66] X. Dai, H. Xie, H. Wang, C. Li, Z. Liu, L. Wu, The geometric phase analysis method based on the local high resolution discrete Fourier transform for deformation measurement, Meas. Sci. Technol., 25 (2014), 025402.

[67] L. Li, Z. Gan, M.R. McCartney, H. Liang, H. Yu, Y. Gao, J. Wang, D.J. Smith, Atomic configurations at InAs partial dislocation cores associated with Z-shape faulted dipoles, Scientific Report, 3229 (2013), pp:1-5.

[68] G.S. Was, Irradiation hardening and deformation, Fundamentals of Radiation Materials Science Metals and Alloys, second ed., Berlin Springer (2017), pp: 716-719.

[69] B. Fultz, J. Howe, Transmission Electron Microscopy and Diffractometry of Materials, Fourth edition, Springer, 2013.

[70] D.B. Williams, C.B. Carter, Elastic Scattering, Transmission Electron Microscopy, second ed., New York, 2009, pp: 39-42.

[71] S.R.de Debiaggi, M. de Koning, A.M. Monti, Theoretical study of the thermodynamic and kinetic properties of self-interstitials in aluminum and nickel, Phys. Rev. B, 73 (2006), 104103.

[72] https://www.totalresolution.com/CrystalKit.html.

[73] https://www.totalresolution.com/MacTempasX.htm.

[74] D.B. Williams, C.B. Carter, High-Resolution TEM. Transmission Electron Microscopy, second ed., New York, 2009, pp: 483-506.

[75] D. Zhou, F. Qiu, Q. Jiang, Simultaneously increasing the strength and ductility of nano-sized TiN particle reinforced Al-Cu matrix composites, Mater. Sci. Eng. A, 596 (2014), pp: 98-102.

[76] K.N. Goswami, A. Mottura, A kinetic Monte Carlo study of vacancy diffusion in non-dilute Ni-Re alloys, Mate. Sci., Eng. A, 743 (2019), pp: 265-273.

[77] Y.A. Sherider, The Monte Carlo Method in chapter I Principles of the Monte Carlo method, (1966), pp: 1-90.

[78] W. Yang, R. Dong, L. Jiang, G. Wu, M. Hussain, Unstable stacking faults in submicron/micron Al grammins in multi-SiCp/multi-Al nanocomposite, Vacuum, 122 (2015), pp: 1-5.

[79] G.S. Was, Deformation in Irradiated Metals, Fundamentals of Radiation Materials Science Metals and Alloys, second ed., Berlin Springer (2017), pp: 716-719.

[80] G. Das, J. Washburn, Defects formed from excess vacancies in aluminum, Philos. Mag., 11 (1965), pp: 955-967.

[81] D.S. Gelles, Effects of stress on microstructural evolution during irradiation, J. Nucl.

Mater., 205 (1993), pp: 146-161.

[82] A.J.E. Foreman, J. V. Sharp, A mechanism for the sweeping-up of loops by glide dislocations during deformation, Philos. Mag., 19 (1969), pp: 931-937.

[83] H. Tanigawa, A. Kohyama, Y. Katoh, A modeling of radiation induced microstructural evolution under applied stress in austenitic alloys, J. Nucl. Mater., 239 (1996), pp: 80-84.

[84] D.B. Williams, C. B. Carter, Elastic scattering, Transmission Electron Microscopy, second ed., New York, 2009, pp: 39-49.

[85] E. Abe, Atomic-Scale Characterization of Nanostructured Metallic Materials by HAADFZ-contrast STEM, Mater. Trans., 44 (2003), pp: 2035- 2041.

[86] T.J. Konno, M. Kawasaki, K. Hiraga, Guinier-Preston zones observed by high-angle annular detector dark-field scanning transmission electron microscopy, Philos. Mag., 81 (2001), pp: 1713-1724.

[87] L. Bourgeois, C. Dwyer, M. Weyland, J.F. Nie, B.C. Muddle, Structure and energetics of the coherent interface between the θ^' precipitate phase and aluminum in Al-Cu, Acta Mater., 59 (2011), pp: 7043-7050.

[88] Z. Shen, Q. Ding, C. Liu, J. Wang, H. Tiana, J. Li, Z. Zhang, Atomic-scale mechanism of the θ" → θ" phase transformation in Al-Cu alloys, J. Mater. Sci. Technol., 33 (2017), pp: 1159-1164.

[89] A.B. Bortz, M.H. Kalos, J.L. Lebowitz, A New Algorithm for Monte Carlo Simulation of Ising Spin Systems, J. Comput. Phys., 17 (1975), pp: 10-18.

[90] C.V. Singh, D.H. Warner, Mechanisms of Guinier-Preston zone hardening in the athermal limit, Acta Mater., 58 (2010), pp: 5797-5805.

Acknowledgement

When I start writing the acknowledgement, I have just realized that my PhD journey at Tohoku University is coming to an end. These four years in Tohoku University trained me to be an early career researcher with generous support from my supervisors, colleagues, friends and family. The thesis would not be possible to be accomplished without your help and I won my deepest debt of gratitude to all of you!

Firstly, I would like to express my deepest gratitude to my supervisors, working with them is a great fortune to me during the study at the Oarai. I would like to express my deepest appreciation to my principal supervisor Prof. Yasuyoshi Nagai for his thoughtful and patient supervision, as well as his encouragement whenever I felt confused in my study and life. I was so grateful to his words that cheered me up when I failed in the first confirmation. I would also like to express my gratitude to Profs. Koji Inoue and Kenta Yoshida, my associate supervisors. They have been extraordinarily inspiring and informative for my study and research, offering professional guidance and warm encouragement. I still remember the constructive recommendation notes on my thesis chapters and other paper works that carefully written word by word. I also want to thank my co-supervisor Professor Somei Ohnuki who met me during my mater study in Beijing. His professional suggestions and advice inspired me at some difficult stages of this thesis in Tohoku University. I also express my gratitude to all the friendly colleagues and staffs at the Tohoku University center of Oarai, especially Ms. Okuno, Ms. Shibahara, Mr. Kurano, Ms. Kume, Ms. Tomura, Mr. Suzuki and Mr. Maniwa. Thanks to Yufeng Du, Huichao Liang, Jie Ren, Pengfei Liu, Can Zhao, Miyata and many other PhD candidate comrades for their valuable comments and generous help.

Gratefulness is also given to Professor Suzudo, who gave me strong advice and support

every time I met troubles in simulation. During the process of writing my first journal paper to magazine, I would like to express my gratitude to Professor Konno from Tohoku University and those anonymous reviewers gave me constructive advice. I would like to thank Prof. Akira Hasegawa and Prof. Ryuta Kasada for their fruitful suggestion to revise the manuscript. I would like to thank Assistant Prof. Yusuke Shimada for helping me with the experiment and discussions for my study.

This research would not have completed without contributions of the many people who guided the process of data collection. I want to thank all of the audiences and leaders of science society for contributing their time and energy to this research, as well as Nishitani who introduced the history of Al material and gave me help during the fieldwork.

I should thank my parents for their deep love, encouragement and support in my studies and life. I still remember when I was harassed by people, what they said to me was: if it is really difficult that difficult to overcome, come back to home, we also can live without a doctor's degree, we can't lose our physical and mental health because of a PhD degree. They did not say that being hard on you is for your own good. You have to learn to endure, learn to bear, and overcome all the difficulties by yourself. It is they who give me the space to retreat, so that I do not choose extreme solutions when I meet difficulties, such as suicide. I sincerely wish them to enjoy their life in good health. Thanks to my friends Yufeng Du, Huichao Liang, Jie Ren, Pengfei Liu, Can Zhao and many other friends I met in Tohoku University. I really appreciate the happy days with you. Thanks to ‘Happy Friday’, a party in international house, that gave me spirit support and smell enjoying during every week. Good to see you in China as an unforgettable memory and wish everybody with a happy ending soon. Appreciation also gives to those kind-hearted and supportive friends online who I have met or even never met yet.

The Chinese government would be specially thanked for providing me the scholarship during the PhD study. I would also like to express my gratitude to owner of seven eleven convenient store Mr. Ishizaki, my boss of pastime. He gave me a job on my pass time and gave me a financial support. I also want to thank my co-workers Ms. Watanabe, Mr. Ayumu, Mr. Hiroki, who are staffs of seven eleven convenient store. They shared their experience of work and life in convenient store, and they also talk to me about their interesting things.

At the end of the acknowledgement, I would lastly thank myself who complete with loneliness and overcome every difficulty along with great passion and depression during the PhD journey. I believe that what doesn't kill me makes me stronger and be a better girl.

January 21, 2022 @ Oarai, Japan

Jiao CHEN